PHYSICAL REVIEW FLUIDS **9**, 074609 (2024)

Reactive Rayleigh-Taylor turbulence: Influence of mixing on the growth and displacement of the mixing zone

Kevin Ley,[*] Olivier Soulard,[†] Jérôme Griffond, and Antoine Briard
CEA, DAM , DIF, F-91297 Arpajon, France

Serge Simoëns
École Centrale de Lyon, MFAE, LMFA, F-69134 Écully, France

(Received 23 February 2024; accepted 26 June 2024; published 25 July 2024)

The purpose of this paper is to investigate the effects of molecular mixing on the evolution of a reactive Rayleigh-Taylor turbulent mixing zone. In this regard, we derive algebraic relations showing that an increase in the mixing level leads to a slowing of the growth of the mixing zone width. We also show the existence of a maximum displacement velocity of the mixing zone center. These predictions are assessed using both direct numerical simulations and large eddy simulations.

DOI: 10.1103/PhysRevFluids.9.074609

I. INTRODUCTION

The Rayleigh-Taylor instability occurs when two fluids initially separated by an interface are submitted to an acceleration pointing from the denser fluid to the less dense one [1–5]. In this configuration, the small perturbations seeding the initial interface are amplified and eventually develop into a turbulent mixing zone. At late times, this zone reaches a self-similar regime such that its width increases as the square of time. The prefactor α_{nr} of this quadratic evolution is a key parameter of Rayleigh-Taylor turbulence and has been the object of numerous studies [6–17] (note that the subscript "nr" in α_{nr} stands for nonreactive). Among these studies, several point out that α_{nr} is connected to the level of molecular mixing reached in the flow [7–12]. Indeed, the less mixing there is, the more potential energy is available and the faster the growth of the mixing zone should be. As a result, α_{nr} is expected to increase as the level of mixing decreases. This intuitive idea was given a quantitative formulation in Refs. [11,12]. In these two works, α_{nr} was shown to be a decreasing function of the global mixing parameter Θ, a ratio equal to 0 when the flow is fully segregated and to 1 when it is fully mixed.

In the present work, we consider a Rayleigh-Taylor mixing zone in which chemical or fusion reactions take place [18–34]. Our purpose is to understand whether the level of molecular mixing influences the self-similar evolution of this reactive layer, as it does for a nonreactive one. This question is of importance for several applications, such as type Ia supernovae [27–34]. In the latter context, several authors have proposed idealized configurations of Rayleigh-Taylor unstable flames in order to better understand the physical mechanisms at work in these flows. One of the simplest possible setting, studied, for instance, in [30–34], consists in a statistically planar flame with a small density contrast that propagates upward in a gravity field. The flame is piloted by a single isothermal reaction and consumes heavy reactants initially placed on top of light products. At late times, this unstable flame becomes turbulent, and its brush can equivalently be viewed as a turbulent mixing

---

[*] Also at École Centrale de Lyon, MFAE, LMFA, F-69134 Écully, France.
[†] Also at Université Paris-Saclay, CEA, LMCE, Bruyères-le-Châtel 91680, France.

zone driven by the interplay between the Rayleigh-Taylor instability and combustion. It is this idealized flow that we will hereafter examine and refer to as reactive Rayleigh-Taylor turbulence.

The numerical and theoretical studies of [30–33] have put forward several key features of reactive Rayleigh-Taylor turbulence. First, a self-similar regime is reached at late times, such that the width of the mixing zone grows quadratically with time. This is similar to the nonreactive case, except that the prefactor α of this quadratic growth is not necessarily equal to the nonreactive prefactor α_{nr}. Another difference with the nonreactive case is that the center of the mixing zone is not stagnant: it moves towards the reactants as they are being consumed. At late times, the distance traveled by the center is again proportional to the square of time with a prefactor β different from α and α_{nr}. A last key feature highlighted in [30] is that reactions take place in thin flame fronts that separate pockets of pure fluids. The typical size of these fronts increases with time but at a much slower rate than the size of the mixing zone. As a result, the proportion of the volume occupied by mixed regions decreases, and the flow becomes more and more segregated: the mixing parameter Θ tends to 0. This is strikingly different from the nonreactive case where high levels of mixing are generally observed with Θ reaching nonzero asymptotic values as high as 0.8 [16].

This last property raises an apparent conundrum concerning the objective of this paper. Indeed, for the nonreactive case, we mentioned that the growth rate of the mixing zone α_{nr} is connected to the level of mixing measured by the value of the mixing parameter Θ [11,12]. But for the reactive case, the existence of such a dependency appears elusive: the level of mixing vanishes and Θ decreases to 0 whatever the value of the growth rate α. The asymptotic values of α and Θ are consequently independent, and, at first sight, it seems that the connection between α and the level of mixing is lost. However, if Θ always tends to 0, it does so in a self-similar fashion, proportionally to the inverse of time and to a nondimensional parameter γ [30]. Hence, at a given time and for a given reaction rate, a higher γ implies a higher level of mixing. In other words, the mixedness of a self-similar reactive Rayleigh-Taylor flow is measured by the nonzero constant γ and not by the vanishing value of Θ. With this understanding, looking for a dependency of α on the level of mixing remains as legitimate in reactive Rayleigh-Taylor turbulence as it is in the nonreactive case [7–12], provided one substitutes γ to Θ as a measure of the level of mixing. Furthermore, if the growth rate α depends on γ, one may also wonder if it is also the case for the coefficient β measuring the displacement of the mixing zone center.

Thus, the main question we would like to examine in this work can be rephrased as follows: do the growth and displacement rates, α and β, of a self-similar reactive Rayleigh-Taylor mixing zone exhibit any dependency on the degree of mixing of the flow as measured by the constant γ? To answer this question, we turn our attention to nonreactive Rayleigh-Taylor turbulence and to the $\alpha_{\mathrm{nr}} - \Theta$ relation derived in [11,12]. Two broad assumptions are required to obtain this relation and none of them is specifically tied to the nonreacting character of the flow. Hence, in this work, we propose to start from the very same assumptions as in [11,12] and to follow their consequences but this time in a reactive setting. More precisely, we assume that an eigenmode of the buoyancy production term is dominant over the other ones and that second-order moments are known functions of the mean concentration. Equipped with these hypotheses, we are then able to explore how α, β, and γ are related.

This paper unfolds as follows. In Sec. II a general description of reactive Rayleigh-Taylor turbulence, along with its governing equations, is given. Then in Sec. III the two assumptions mentioned above are detailed, and relationships between α, β, and γ are derived. Finally, in Sec. IV direct numerical simulations (DNS) and large-eddy simulations (LES) are performed. The resolution of these simulations is high enough to attain a state close to self-similarity. Hence, the validity of the results derived in Sec. III can be assessed with these simulations.

II. GENERAL DESCRIPTION OF REACTIVE RAYLEIGH-TAYLOR TURBULENCE

In the introduction, we gave a brief definition of reactive Rayleigh-Taylor turbulence and outlined some of its properties. The aim of this section is to provide further details on this idealized configuration. More precisely, we present the governing equations of reactive Rayleigh-Taylor turbulence, describe its self-similar regime, and draw comparisons with the nonreactive case.

A. Governing equations and global flow parameters

We consider two incompressible fluids that mix and react, while being submitted to a destabilizing gravity field pointing in the direction $\boldsymbol{x}_3$. We assume that the Atwood number of the mixing zone—defined as $\mathtt{A}_t = (\rho_h - \rho_l)/(\rho_h + \rho_l)$, with $\rho_{h,l}$ the densities of the "heavy" and "light" fluids—is small compared to one. Also, for the sake of simplicity, we restrict our attention to the case where the heavy fluid reacts with the light fluid to give even more light fluid. This reaction is autocatalytic and can be described by adding a Fischer-Kolmogorov-Petrovsky-Piskunov (F-KPP) source term to the evolution of the concentration of the light fluid. Autocatalytic reactions, and their interaction with the Rayleigh-Taylor instability, play an important role in many industrial applications [18–23]. The system studied here is consequently directly relevant to these situations. Beyond this aspect, single-step auto-catalytic reactions can also be viewed as toy models for both premixed and nonpremixed combustion (see [30] for a discussion on this subject). This property has been used to gain insights into the behavior of RT unstable flames and in particular those appearing in SNIa progenitors [27–34]. However, it should be emphasized that a single-step reaction which involves only one scalar cannot describe a configuration where the progress of the reaction is decoupled from the advancement of mixing. At least two scalars would be required in that case. This situation may occur in a wide variety of contexts including some inertial confinement fusion experiments [25,26,35]. The study of such configurations is beyond the scope of this work. Note that this limitation is not linked to the particular dependency of the F-KPP source term on the concentration field. The results obtained in this article can be adapted to more complex dependencies, as explained in Appendix C.

Within this framework, the evolution of the velocity and concentration fields is governed by the following reactive Boussinesq equations:

$$\partial_t c + u_k \partial_k c = \nu_c \partial^2_{kk} c + \frac{1}{\tau} c(1-c), \tag{1a}$$

$$\partial_t u_i + u_k \partial_k u_i = -\partial_i p + \nu \partial^2_{kk} u_i + 2\mathtt{A}_t g c \delta_{i3}, \tag{1b}$$

$$\partial_k u_k = 0, \tag{1c}$$

with $\boldsymbol{u}$ the velocity field, c the concentration of the light products, g the gravity, p the reduced pressure, ν and ν_c the viscosity and diffusion coefficients, and τ the characteristic time of the reaction. In the absence of a turbulent velocity field ($\boldsymbol{u} = 0$), a laminar flame propagates with a typical velocity s_{lam} and length δ_{lam} defined by

$$s_{\text{lam}} = 2\sqrt{\nu_c/\tau} \quad \text{and} \quad \delta_{\text{lam}} = 8\sqrt{\nu_c \tau}. \tag{2}$$

To complete Sys. (1), initial conditions must be provided. Here we assume that the light and heavy fluids are initially separated by an interface centered around the position $x_3 = 0$ and deformed by a perturbation of height $h(x_1, x_2)$. With $\mathtt{A}_t g > 0$, the flow is Rayleigh-Taylor unstable provided $c = 1$ for $x_3 < h$ and $c = 0$ for $x_3 > h$:

$$c(\boldsymbol{x}, t = 0) = \text{Heaviside}[h(x_1, x_2) - x_3]. \tag{3}$$

This corresponds to having heavy reactants initially placed above light products. As a result of this convention, the flame propagates towards positive x_3, and the gradient of the mean concentration is negative.

A typical evolution of a reactive Rayleigh-Taylor flow obeying Sys. (1) and starting from initial condition (3) is shown in Fig. 1. This figure displays the volume rendering of the concentration field extracted at three different times for simulation D2 that will be detailed in Sec. IV. As we can see, not only does the width L of the mixing zone increase, but its center X_c is also displaced as reactants

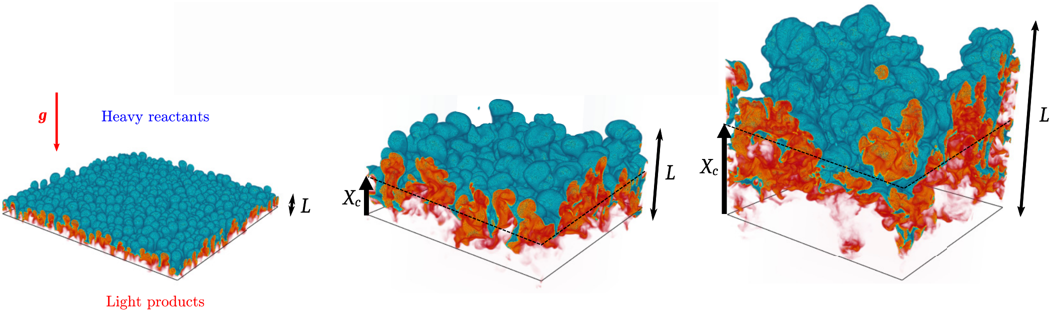

FIG. 1. Typical evolution of a reactive Rayleigh-Taylor flow. Volume rendering of the concentration field c of simulation D2 (see Table I) at times $t = 0.8$, $t = 1.9$, and $t = 2.9$. The rendering is done for $0.01 < c < 0.99$. Red corresponds to $c = 0.99$ (light products) and blue to $c = 0.01$ (heavy reactants).

are consumed. Another important feature of this mixing zone is its high degree of segregation. This can be seen in Fig. 1 by the overwhelming presence of the red and blue colors, which correspond to zones of almost pure fluids.

These three features—width, displacement, and mixing level—can be measured using the following diagnostics:

$$L = 6\int \overline{c}(1-\overline{c})\,\mathrm{d}x_3, \quad X_c = \int (\overline{c}-\overline{c}^{(0)})\,\mathrm{d}x_3, \quad \text{and} \quad \Theta = \frac{\int \overline{c(1-c)}\,\mathrm{d}x_3}{\int \overline{c}(1-\overline{c})\,\mathrm{d}x_3}, \tag{4}$$

where $\overline{\cdot}$ denotes the ensemble mean and where $\overline{c}^{(0)}(x_3) = \overline{c}(x_3, t = 0)$ is the initial value of $\overline{c}$. The parameter Θ is called mixing ratio or mixing parameter. Its value falls within the interval [0, 1], $\Theta = 0$ corresponding to a fully segregated flow and $\Theta = 1$ to a fully mixed one. Note that the mixing zone width L is defined up to a multiplicative constant, here chosen equal to 6. Different values can be found in the literature, and the choice made here could appear to be arbitrary. However, this is not the case. The reason for selecting a prefactor equal to 6 is linked to the assumptions detailed in Sec. III. They lead to a unique unambiguous value of the prefactor, as explained in Appendix A.

B. Self-similarity and combustion regime

At late times, Chertkov *et al.* [30] showed that a reactive Rayleigh-Taylor flow obeying Sys. (1) reaches a self-similar state such that

$$L(t) = 2\alpha \mathrm{A}_t g t^2, \quad X_c(t) = 2\beta \mathrm{A}_t g t^2, \quad \text{and} \quad \Theta(t) = \gamma \frac{\tau}{t}, \tag{5}$$

where α, β, and γ are three dimensionless constants. Another way of specifying this self-similar regime is by defining dynamic estimates of the coefficients α, β, and γ. More precisely, let us introduce the following quantities:

$$\alpha_{\mathrm{L}}(t) = \frac{\dot{L}(t)}{8\mathrm{A}_t g\, \tau_L(t)}, \quad \beta_{\mathrm{L}}(t) = \frac{\dot{X}_c(t)}{8\mathrm{A}_t g\, \tau_L(t)}, \quad \text{and} \quad \gamma_{\mathrm{L}}(t) = 2\Theta(t)\frac{\tau_L(t)}{\tau}, \tag{6}$$

where the notation $\dot{f}(t) = \mathrm{d}_t f(t)$ is used as a shorthand for the time derivative of a function f depending uniquely on t and where τ_L is the time associated with the growth of the mixing zone width L:

$$\tau_L(t) = \frac{L(t)}{\dot{L}(t)}. \tag{7}$$

Then the self-similar regime expressed by Eq. (5) can equivalently be defined by

$$\text{for } t \to \infty, \quad \alpha_{\mathrm{L}}(t) = \alpha, \quad \beta_{\mathrm{L}}(t) = \beta, \quad \text{and} \quad \gamma_{\mathrm{L}}(t) = \gamma. \tag{8}$$

Note that the definition of α_{L} is identical to the one used classically in nonreactive Rayleigh-Taylor flows. It is, however, more commonly written in the form $\alpha_{\mathrm{L}} = (\dot{L})^2/(8\mathtt{A}_t gL)$.

Two aspects of the self-similar regime given by Eq. (5) [or equivalently Eq. (8)] are worth highlighting. The first one is that $\mathtt{A}_t g$ and t are the only dimensional parameters appearing in the expressions of L and X_c. This implicitly means that buoyancy forces are the primary mechanism driving the growth and displacement of the mixing zone. Nonetheless, the influence of reactions must not be ruled out: they can still have an impact on L and X_c through the values of the constants α and β.

The second remarkable point is that Θ tends to 0, that is, the flow becomes more and more segregated with time. In [30], this behavior was associated with the emergence of a thickened-wrinkled flame combustion regime [36]. As its name indicates, this regime corresponds to reaction zones that are broadened by the smallest scales of the turbulent spectrum, while also being wrinkled by the largest ones. Chertkov *et al.* [30] showed that, in reactive Rayleigh-Taylor turbulence, the broadening of the reaction zones is slower than the growth of the mixing zone width. Hence, the volume they occupy becomes smaller and smaller compared to the volume occupied by the burnt and unburnt fluids. This results in Θ tending to 0.

It should be emphasized that the tendency towards the thickened-wrinkled regime is a direct consequence of the self-similar evolution expressed by Eq. (5). More precisely, the thickened-wrinkled flame regime is defined by high values of two nondimensional numbers, the Damköhler and Karlovitz numbers, which compare the reaction time τ to the characteristic times τ_t and τ_η of the largest and smallest structures of the turbulent field. These two numbers are defined as $\mathtt{Da} = \tau_t/\tau$ and $\mathtt{Ka} = \tau/\tau_\eta$. During the self-similar phase, with $\mathtt{A}_t g$ and t the only dimensional parameters involved, we necessarily have $\tau_t \propto t$. Furthermore, assuming a Kolmogorov turbulent spectrum, we have $\tau_\eta \propto \tau_t \mathtt{Re}^{-1/2} \propto t^{1/2}$, with $\mathtt{Re}$ the turbulent Reynolds number. Therefore, once the self-similar phase is reached, $\mathtt{Da}$ and $\mathtt{Ka}$ grow with time and eventually become very large: the thickened-wrinkled flame regime is reached.

This property can be illustrated using a Borghi diagram, which allows us to visualize the different combustion regimes in a velocity-length scale phase space. Figure 2 shows such a Borghi diagram in which the typical turbulent velocity v' and length scale ℓ_t at the center of the mixing zone and for different times are reported for simulations D1, D2, D3, and D4 detailed in Sec. IV. Once self-similarity is reached, we have $v' \propto t$ and $\ell_t \propto t^2$ so that $v' \propto \ell_t^{1/2}$. In other words, a self-similar evolution of these quantities appears in the Borghi diagram as a curve with a logarithmic slope 1/2. This property is indeed observed for simulations D1, D2, D3, and D4 in Fig. 2. It can also be observed in this figure that a 1/2-slope curve always ends up within the boundaries of the thickened-wrinkled flame region as time increases. This region is indeed delimited by the two curves $\mathtt{Da} = 1$ and $\mathtt{Ka} = 1$, which respectively have logarithmic slopes of 1 and 1/3.

C. Comparison with nonreactive Rayleigh-Taylor turbulence

Without reaction, the self-similar state of Rayleigh-Taylor turbulence is characterized by the following relations:

$$\text{Nonreactive case: } L = 2\alpha_{\mathrm{nr}}\mathtt{A}_t g t^2, \quad X_c = 0, \quad \text{and} \quad \Theta = \Theta_\infty, \tag{9}$$

where α_{nr} and Θ_∞ are dimensionless constants.

The comparison between Eqs. (5) and (9) reveals several differences between reactive and nonreactive Rayleigh-Taylor turbulence. First, even though the growth of the mixing zone is quadratic in time in both cases, the growth constants α and α_{nr} of the two flows are not necessarily the same. Second, the center of the mixing zone does not move in the absence of reaction. And, finally, without reactions, the mixing parameter Θ tends to a nonzero constant Θ_∞. Simulations [4] suggest that Θ_∞ is close to 0.8, which corresponds to a well-mixed flow. This is in stark contrast with the reactive case for which the mixture becomes almost fully segregated. This last point, more than any other, sets apart the reactive and nonreactive versions of the Rayleigh-Taylor instability.

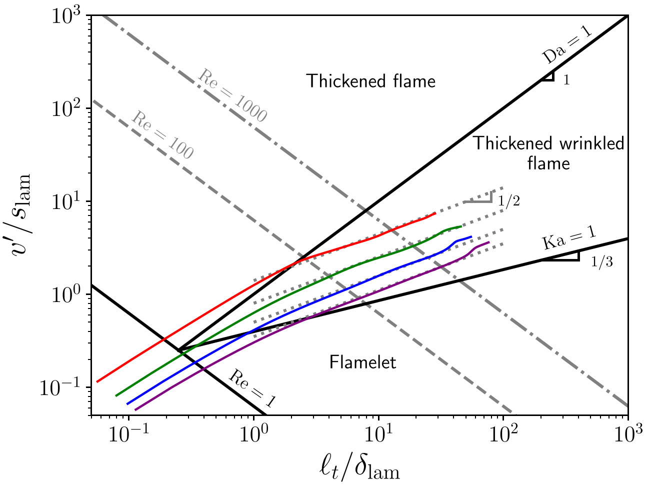

FIG. 2. Borghi diagram for simulations D1 (red), D2 (green), D3 (blue), and D4 (purple) (see Table I for simulation names). The curve shown for each simulation is obtained by plotting $[\ell_t(t)/\delta_{\mathrm{lam}}, v'(t)/s_{\mathrm{lam}}]$ for different times t. The turbulent velocity v' corresponds to the square root of the turbulent kinetic energy taken at the center of the mixing zone. The integral scale ℓ_t is computed by integrating the turbulent velocity spectrum divided by the wave number and normalized by the kinetic energy. The definitions of the laminar flame speed and width are given in Eq. (2).

Indeed, mixing plays an important role in understanding the behavior of Rayleigh-Taylor turbulence. As explained in the introduction, a lesser level of molecular mixing implies that more potential energy is available and can be converted into kinetic energy, which, in turn, can contribute to the growth of the mixing zone. This simple and intuitive reasoning connects the growth of the mixing zone to the level of mixing. It does not depend on whether reactions are present or not and, if verified, should apply equally well to nonreactive and reactive Rayleigh-Taylor turbulence.

For nonreactive Rayleigh-Taylor turbulence, this connection has been corroborated and translated in the form of a relation between the dynamic evaluation α_{L} of the growth coefficient [Eq. (6)] and the mixing parameter Θ [11,12]:

$$\alpha_{\mathrm{L}}(t) = \frac{\{d_{cc}[1-\Theta(t)]\}^2}{1+d_{cc}[1-\Theta(t)]}. \tag{10}$$

At large times, we have $\alpha_{\mathrm{L}}(t) \to \alpha_{\mathrm{nr}}$ and $\Theta(t) \to \Theta_\infty$ so that the asymptotic version of Eq. (10) is

$$\alpha_{\mathrm{nr}} = \frac{[d_{cc}(1-\Theta_\infty)]^2}{1+d_{cc}(1-\Theta_\infty)}. \tag{11}$$

In formulas (10) and (11), $d_{cc} \in [0, 1]$ is an anisotropy coefficient which measures whether turbulent structures are flat or elongated. It is equal to $\pi/4$ in the isotropic case and to 1 for fully elongated structures. A value of 0.7 to 0.8 is generally observed in nonreactive Rayleigh-Taylor simulations [11,12]. In [11], d_{cc} is approximated by $d_{cc} = \int E_{cc}(\boldsymbol{k}) \sin^2\theta \, \mathrm{d}\boldsymbol{k} / \int E_{cc}(\boldsymbol{k}) \, \mathrm{d}\boldsymbol{k}$ where E_{cc} is the concentration spectrum, $\boldsymbol{k}$ the wave number and $\theta = \arccos(k_3/k)$ the angle between $\boldsymbol{k}$ and $\boldsymbol{x}_3$. In [12] a more complex formula involving eigenmode spectra is used.

Equation (10) is assessed in Fig. 3 using the nonreactive Rayleigh-Taylor simulations described in Sec. IV. It can be seen that the simulation results align with the predicted curve defined by Eq. (10) with $d_{cc} = 0.7$. In addition to these nonreactive data, Fig. 3 also displays results for the reactive simulation D2 described in Sec. IV. As expected from Eqs. (5) and (9), the $(\alpha_{\mathrm{L}}, \Theta)$ trajectories of the reactive and nonreactive cases are blatantly different, and formula (10) clearly does not apply to reactive Rayleigh-Taylor turbulence. In the reactive case, an almost horizontal line is obtained: α_{L}

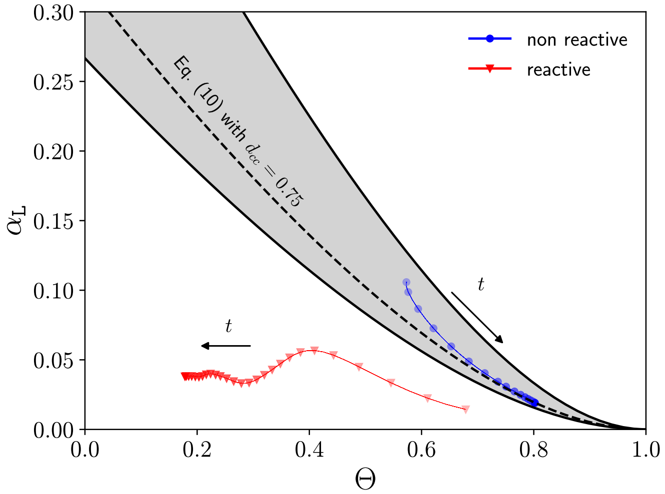

FIG. 3. Comparison between reactive (Sim. D2) and nonreactive (Sim. NR) Rayleigh-Taylor turbulence (see Table I for simulation names). Growth coefficient α_L as a function of the mixing parameter Θ for an interval of time such that L/L_{dom} varies between 0.02 and 0.3 for Sim. D2 and between 0.05 and 0.3 for Sim. NR. The opacity of the symbols increases with time. The two black curves are obtained by setting $d_{cc} = 1$ and $d_{cc} = 2/3$ in Eq. (10). The gray region they delimit corresponds to the ($\alpha_L - \Theta$) domain identified in [11] as encompassing most simulation and experimental results of nonreactive Rayleigh-Taylor turbulence.

reaches an asymptotic value, while Θ still decreases with time. This horizontal line is an illustration of the fact that no univocal relation between α_L and Θ can be drawn in the reactive case.

At first sight, this observation may appear to contradict the existence of a connection between growth rate and mixing levels in the reactive case. However, it shows only that this connection does not take the form of a $\alpha_L - \Theta$ relationship. Given the properties (5) of the reactive self-similar state, α_L and its asymptotic value α still appear as proper parameters for estimating the growth of the mixing zone. However, the fact that Θ tends to 0 means that this parameter is not fit for comparing mixing levels. Instead, it is the prefactor γ of the decay law of Θ that now plays this role: at a given nondimensional time t/τ, different values of γ imply different degrees of mixing.

Thus, for reactive Rayleigh-Taylor turbulence, the link between growth rate and mixing should not be looked for in the form of a relation between α and Θ but rather between α and γ, or equivalently between α_L and γ_L, the dynamic estimates of α and γ (Eq. (6)). The same remark also applies to β and β_L. To derive these relations, several hypotheses are required. They are detailed in the next section, along with their consequences.

III. RELATIONSHIPS BETWEEN α, β AND γ

A. Overview of the derivation

1. Main steps of the derivation

The derivation presented in this section hinges around one central quantity: the mean concentration $\overline{c}$. The latter evolves according to the following equation, obtained by averaging Eq. (1a):

$$\partial_t \overline{c} + \partial_3 \overline{u_3' c'} = \nu_c \partial_{33}^2 \overline{c} + \frac{1}{\tau} \overline{c(1-c)}, \tag{12}$$

with $X' = X - \overline{X}$ the fluctuation of a given quantity X. The reason why $\overline{c}$ plays such an important role is because the knowledge of its self-similar properties allows us to formulate two independent equations linking α, β, and γ. It thus brings an answer to the problem raised in the preceding section, namely, finding how the growth and displacement rates of the mixing zone, α and β, depend on the mixing level measured by γ.

The first of these two equations is obtained rather straightforwardly. By integrating Eq. (12) over x_3, the following equation for X_c is derived:

$$\dot{X}_c = \frac{\Theta L}{6\tau}, \tag{13}$$

where we used the definitions of X_c, Θ, and L [Eq. (4)] and the fact that the molecular and turbulent concentration fluxes are null outside the mixing zone. Injecting the self-similar evolution of X_c, Θ,and L [Eq. (5)] into this equation, we then find that

$$\beta = \frac{\gamma}{12}\alpha. \tag{14}$$

As for the second relation, its starting point rests on the following observation: once self-similarity is reached, the mean concentration profile depends only the dimensionless coordinate x_3/L and on nondimensional self-similar parameters. These include α, β, and γ but are not limited to them. This property can be expressed as

$$\text{Self-similar regime: } \overline{c}(t, x_3) \equiv \overline{c}_{\mathrm{s}}\left(\frac{x_3}{L(t)}; \alpha, \gamma, \mathbf{p}\right), \tag{15}$$

where $\mathbf{p} = (p_1, p_2, \dots)$ stands for the ensemble of the self-similar parameters other than α and γ. The parameter β is not included due to its explicit dependency on α and γ [Eq. (14)]. When injecting this expression into the definition (4) of L, i.e., into $L = 6\int \overline{c}(1-\overline{c})\mathrm{d}x_3$, and when replacing the integration variable by $y = x_3/L$, we derive that

$$\mathcal{I}(\alpha, \gamma, \mathbf{p}) = 1 \tag{16a}$$

$$\text{with} \quad \mathcal{I}(\alpha, \gamma, \mathbf{p}) = 6\int \overline{c}_{\mathrm{s}}(y; \alpha, \gamma, \mathbf{p})[1 - \overline{c}_{\mathrm{s}}(y; \alpha, \gamma, \mathbf{p})]\mathrm{d}y. \tag{16b}$$

Thus, an integral equation is obtained, which links α, γ and the other self-similar parameters $\mathbf{p}$ together. When solved, this equation allows to express α as a function of γ and $\mathbf{p}$:

$$\alpha \equiv \alpha_s(\gamma, \mathbf{p}). \tag{17}$$

Formally, this solution would answer the main question raised in our paper.

2. Main assumptions

To sum up, Eq. (17) is the main relation we aim to derive. To this end the value of $\mathcal{I}(\alpha, \gamma, \mathbf{p})$ must first be found. For this, it is necessary to determine the self-similar profile $\overline{c}_{\mathrm{s}}$ of $\overline{c}$. This may be accomplished only by introducing simplifying assumptions. In this regard, it is instructive to consider the nonreactive case and the way Eqs. (10) and (11) were obtained in [11,12]. In these references, two main hypotheses were necessary to arrive at these predictions. The first one is that buoyancy production plays a dominant role at energetic scales, and the second that the spatial profile of the mean concentration $\overline{c}$ is linear within the mixing zone. In [11] it was also explained how this second hypothesis is fully equivalent to specifying that the spatial profiles of the variance and flux of concentration are proportional to $\overline{c}(1-\overline{c})$.

Concerning the reactive case, we already noted in Sec. II B that buoyancy forces are the main mechanism driving the growth and displacement of the mixing zone, as implied by the dimensional parameters appearing in the self-similar laws (5). This suggests that the first hypothesis mentioned above should remain appropriate for analyzing reactive Rayleigh-Taylor turbulence. As for the second hypothesis, its alternative formulation based on second-order moments can be viewed as a truncation of their spatial profiles in terms of Legendre polynomials. Its principle is consequently not restricted to the nonreactive case and its implications can also be explored in a reactive context.

Thus, despite the intrinsic differences between reactive and nonreactive Rayleigh-Taylor flows, the study of the way growth rate and mixing are linked can be approached using the same general assumptions. These assumptions, however, have very different consequences in each context. This is what we detail in the remainder of this section.

B. First assumption: Truncated Legendre polynomial expansion

1. Legendre expansion

First, let us recast the evolution equation of $\overline{c}$ by using the self-similar coordinate $y = x_3/L$, already introduced in the definition of $\mathcal{I}(\alpha, \gamma, \mathbf{p})$. We obtain

$$\tau_L \partial_t \overline{c} - y\partial_y \overline{c} + \partial_y(\overline{u_3'c'}/V_L) = \frac{1}{\mathtt{Sc}\,\mathtt{Re_L}} \partial^2_{yy}\overline{c} + \mathtt{Da_L}\,\overline{c(1-c)} \tag{18}$$

$$\text{with} \quad V_L = \dot{L}, \quad \mathtt{Sc} = \frac{\nu}{\nu_c}, \quad \mathtt{Re_L} = \frac{LV_L}{\nu}, \quad \text{and} \quad \mathtt{Da_L} = \frac{\tau_L}{\tau}. \tag{19}$$

We recall that $\tau_L = L/V_L$ has already been introduced in Eq. (7) in order to define α_{L}, β_{L} and γ_{L}. Three nondimensional numbers appear in Eq. (18): the Schmidt number $\mathtt{Sc}$, the Reynolds number $\mathtt{Re_L}$, and the Damköhler number $\mathtt{Da_L}$. The last two are based on the width L and on the velocity $V_L = \dot{L}$ and are different from the turbulent Reynolds and Damköhler numbers, $\mathtt{Re}$ and $\mathtt{Da}$, which were introduced in Sec. II.

By itself, Eq. (18) is not sufficient to make any statement about the shape of $\overline{c}$. Two unknown correlations, the flux of concentration $\overline{u_3'c'}$ and its variance $\overline{c'^2} = \overline{c}(1-\overline{c}) - \overline{c(1-c)}$, are indeed involved in Eq. (18). In order to deal with these correlations, we note that, within the bounds of the mixing zone, the mean concentration $\overline{c}(t, y)$ varies monotonically as a function of y. Hence, within these bounds, i.e., for $0 < \overline{c}(t, y) < 1$, we may invert the dependency of $\overline{c}(t, y)$ on y and write that y is a function of $\overline{c}$:

$$\text{for} \quad 0 < \overline{c} < 1, \quad y \equiv f(t, \overline{c}). \tag{20}$$

Plugging this dependency into the two unknown correlations, we obtain that

$$\text{for} \quad 0 < \overline{c} < 1, \quad \frac{\overline{u_3'c'}}{V_L} = F(t, \overline{c}), \quad \text{and} \quad \overline{c(1-c)} = V(t, \overline{c}). \tag{21}$$

With $\overline{u_3'c'}$ a function of $\overline{c}$, the turbulent transport term of Eq. (18) can be recast in the form of an advection term, with an advection velocity equal to $F'(t, \overline{c}) = \partial_{\overline{c}} F(t, \overline{c})$. Then, in order for the edges of the mixing zone to move at a nonzero finite velocity, F' must tend to a nonzero finite value when $\overline{c} \to 0$ and $\overline{c} \to 1$. As a result, F must be proportional to $\overline{c}$ for $\overline{c} \to 0$ and to $1 - \overline{c}$ for $\overline{c} \to 1$. Furthermore, the Schwartz inequality implies that $\overline{c(1-c)}$ is smaller than $\overline{c}(1-\overline{c})$. Hence, it goes to 0 at most like $\overline{c}$ for $\overline{c} \to 0$ and like $1 - \overline{c}$ for $\overline{c} \to 1$. A general expansion satisfying these boundary conditions can be written using associated Legendre polynomials of order 2:

$$F(t, \overline{c}) = \overline{c}(1-\overline{c})[F_0(t) + F_1(t)\tilde{P}_1(\overline{c}) + \cdots + F_n(t)\tilde{P}_n(\overline{c}) + \cdots], \tag{22a}$$

$$V(t, \overline{c}) = \overline{c}(1-\overline{c})[V_0(t) + V_1(t)\tilde{P}_1(\overline{c}) + \cdots + V_n(t)\tilde{P}_n(\overline{c}) + \cdots], \tag{22b}$$

where $\tilde{P}_n$ is a modified associated Legendre polynomial of second order and degree n:

$$\tilde{P}_n(x) = \sqrt{\frac{(2n+5)n!}{30(n+4)!}}\,\frac{P^{(2)}_{n+2}(2x-1)}{x(1-x)}, \tag{23}$$

with $P^{(2)}_{n+2}$ the actual associated Legendre polynomial of second order and degree $n + 2$.

2. *Truncation of the Legendre expansion*

Expansion (22) does not involve any approximation, and injecting it as such in Eq. (18) would not allow us to make any progress in our derivation: a simplification is needed. This is where we introduce the first of the two major hypotheses mentioned at the beginning of this section. Namely, we assume that the main order of these developments is much larger than the remaining terms:

$$\text{for} \quad i \geqslant 1, \quad F_i \ll F_0, \quad \text{and} \quad V_i \ll V_0. \tag{24}$$

As a result, we propose to approximate the profile of $\overline{u_3'c'}$ and $\overline{c(1-c)}$ by keeping the sole contribution of the main order. Reintroducing y as the dependent variable, this allows to write that

$$\frac{\overline{u_3'c'}}{V_L}(t,y) = \overline{c}(t,y)[1-\overline{c}(t,y)]F_0(t) \quad \text{and} \quad \overline{c(1-c)}(t,y) = \overline{c}(t,y)[1-\overline{c}(t,y)]V_0(t). \tag{25}$$

The coefficient V_0 can be determined by integrating $\overline{c(1-c)}$ over y. Given the definition of Θ in Eq. (4), we straightforwardly find that:

$$V_0(t) = \Theta(t). \tag{26}$$

As for F_0, its expression will be the object of the next section. For the time being, this coefficient can be put aside by introducing a new nondimensional coordinate z defined by

$$z = \frac{y}{2F_0} = \frac{1}{2F_0}\frac{x_3}{L}. \tag{27}$$

3. *Self-similar profile of $\overline{c}$*

We now inject the truncated Legendre expansion (25) into the evolution equation (18) of $\overline{c}$ and use the new coordinate z. But instead of handling directly the equation giving $\overline{c}$ as a function of z, we consider the corresponding equation giving z as a function of $\overline{c}$. As before, this operation is possible because we restrict our attention to the domain $\overline{c}(1-\overline{c}) \neq 0$ where $\overline{c}$ is a strictly monotonic function of z. So, for $0 < \overline{c} < 1$, we derive that $z(t,\overline{c})$ evolves as

$$\tau_L \partial_t z + \frac{\gamma_{\mathrm{L}}}{2}\,\overline{c}(1-\overline{c})\,\partial_{\overline{c}} z = -\left[z(1+\tau_L \dot{F}_0/F_0) + \overline{c} - \frac{1}{2}\right] + \frac{1}{4F_0^2\mathtt{Sc}\cdot\mathtt{Re}_{\mathrm{L}}}(\partial_{\overline{c}} z)^{-2}\partial^2_{\overline{c}\,\overline{c}} z. \tag{28}$$

In the self-similar regime, the following relations hold:

$$\partial_t z(t,\overline{c}) = 0, \quad \dot{F}_0 = 0, \quad \mathtt{Re}_{\mathrm{L}} \to \infty, \quad \text{and} \quad \gamma_{\mathrm{L}} = \gamma. \tag{29}$$

As a result, in the self-similar regime, Eq. (28) simplifies to

$$\frac{\mathrm{d}z}{d\overline{c}} = -\frac{2}{\gamma}\frac{z+\overline{c}-\frac{1}{2}}{\overline{c}(1-\overline{c})}. \tag{30}$$

The solution of this equation is

$$z_s(\overline{c};\gamma) = \frac{1}{2} - \frac{2\overline{c}}{2+\gamma}\;{}_2\mathrm{F}_1(1,1;2+2/\gamma;\overline{c}), \tag{31}$$

where ${}_2\mathrm{F}_1(a_1,a_2;b_1;x)$ is the Gauss hypergeometric function with parameters a_1, a_2, b_1 and variable x. By inverting this expression, we eventually obtain $\overline{c}_{\mathrm{s}}$, the self-similar profile of $\overline{c}$, as a function of z and γ:

$$\overline{c}_s(z;\gamma) = z_s^{-1}(z;\gamma). \tag{32}$$

In the general case, finding the inverse z_s^{-1} of z_s cannot be done analytically and requires numerical means. Nonetheless, several remarkable properties of $\overline{c}_{\mathrm{s}}$ can still be put forward. In particular, the range over which $\overline{c}_{\mathrm{s}}$ is strictly different from 0 and 1 extends symmetrically with respect to $z = 0$, from $z = -1/2$ to $z = +1/2$. However, between these symmetric bounds, the self-similar profile

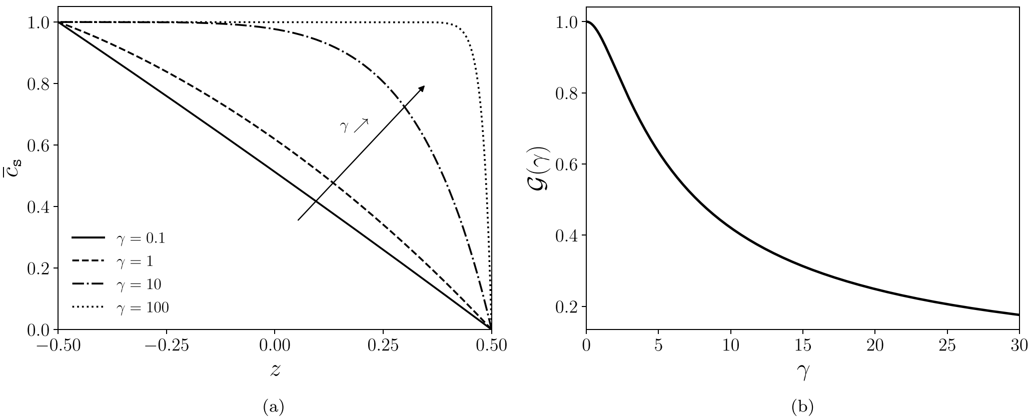

FIG. 4. Self-similar profile of $\overline{c}$ and associated length scale ratio. (a) Self-similar profile of $\overline{c}$ as a function of z for different values of γ. (b) Variation of $\mathcal{G} = L/H$ as a function of γ.

of $\overline{c}$ can be strongly asymmetric, depending on the value of γ. To illustrate this point, we may consider two asymptotic limits : $\gamma \to 0$ and $\gamma \to \infty$. For $\gamma \to 0$, the hypergeometric function ${}_2\mathrm{F}_1(1, 1; 2 + 2/\gamma; \overline{c})$ appearing in Eq. (31) tends to 1 so that the self-similar profile of $\overline{c}$ becomes linear and symmetric with respect to $z = 0$:

$$\text{for} \quad \gamma \to 0, \quad \overline{c}_\mathrm{s} = \tfrac{1}{2} - z. \tag{33}$$

By contrast, when $\gamma \to \infty$, ${}_2\mathrm{F}_1(1, 1; 2 + 2/\gamma; \overline{c})$ tends to $-(\ln(1 - \overline{c}))/\overline{c}$. As a result, we have

$$\text{for} \quad \gamma \to \infty, \quad \overline{c}_\mathrm{s} = 1 - e^{-\frac{\gamma}{4}(1-2z)}. \tag{34}$$

Thus, for large γ, $\overline{c}_\mathrm{s}$ is close to a step: it is almost equal to 1 over most of the interval $[-1/2, 1/2]$ and goes to 0 over a small subinterval located close to $z = 1/2$.

4. The length scales of $\overline{c}_\mathrm{s}$ and their ratio

Figure 4(a) shows how $\overline{c}_\mathrm{s}$ transitions from a linear to a steplike profile with increasing γ. Because of this behavior, a single length scale is not sufficient to characterize the profile of $\overline{c}_\mathrm{s}$. Indeed, as γ increases, the size of the domain where $\overline{c}_\mathrm{s}$ is strictly different from 0 and 1 disconnects from the size of the fast varying front of $\overline{c}_\mathrm{s}$: the ratio between the latter and the former goes to 0.

More precisely, the support of $\overline{c}_\mathrm{s}$ extends from $-1/2$ to $1/2$ in terms of the nondimensional variable $z = x_3/(2F_0L)$. In dimensional units, this means that the total extent of the concentration profile is

$$H = 2F_0L. \tag{35}$$

The definition (4) of L entails that the latter scale measures only the part of the domain where $\overline{c}_\mathrm{s}$ is significantly different from 0 and 1. In other words, L gives a measure of the fast varying front of $\overline{c}_\mathrm{s}$. The ratio between L and H can be evaluated by simply changing the integration variable from x_3 to z in the definition (4) of L. By doing so, we derive that

$$\frac{L}{H} = \mathcal{G}(\gamma) = 6 \int_{-1/2}^{1/2} \overline{c}_\mathrm{s}(z;\gamma)[1 - \overline{c}_\mathrm{s}(z;\gamma)]\,\mathrm{d}z. \tag{36}$$

Changing again the integration variable, this time from z to $c = c_s(z;\gamma)$, we obtain that

$$\mathcal{G}(\gamma) = 6 \int_0^1 c(1-c)\left|\frac{\mathrm{d}z_s}{\mathrm{d}c}\right|(c)\,\mathrm{d}c = \frac{12}{\gamma}\int_0^1 z_s(c;\gamma)\,\mathrm{d}c, \tag{37}$$

where, in the second equality, we used the definition (30) of $\mathrm{d}z_s/\mathrm{d}c$ and the fact that $\int_0^1(c-1/2)\,\mathrm{d}c=0$. Finally, injecting the hypergeometric expression (31) of z_s into this equation, we reach the following result:

$$\mathcal{G}(\gamma)=\frac{6}{\gamma}\left\{1-\frac{4}{\gamma}\left[1-\frac{2}{\gamma}\Psi^{(1)}\left(1+\frac{2}{\gamma}\right)\right]\right\}, \tag{38}$$

where $\Psi^{(1)}(x)=\frac{d^2\ln\Gamma(x)}{dx^2}$ is the trigamma function.

The function $\mathcal{G}$ is displayed in Fig. 4(b). It is strictly decreasing and has values in the interval [0, 1]. It verifies

$$\mathcal{G}(0)=1\quad\text{and}\qquad\text{for}\quad\gamma\gg1,\quad\mathcal{G}(\gamma)=6/\gamma.$$

Thus, the two length scales L and H only coincide for small values of γ. For large values of γ, L becomes much smaller than H: a fast-varying front is formed with a size of order γ^{-1} relative to the total extent of the mixing zone.

An important point is that H gives not only the size of the domain where $\overline{c}\in]0,1[$. It also gives the minimum extent of the region where the turbulent kinetic energy is not null. Otherwise, $\overline{u_3'c'}$ could not be proportional to $\overline{c}(1-\overline{c})$. As a result, for large γ, the size L of the front where $\overline{c}$ varies rapidly becomes much smaller than the size occupied by the turbulent field itself. Also, for large γ, buoyancy production concentrates within the front, which has large mean concentration gradients, and becomes almost null outside of it. Hence, turbulence can be thought to be generated within the front and then left to decay and diffuse outside of it as the front advances.

C. Second assumption: Predominance of the enhanced buoyancy eigenmode

With Eq. (32), we have succeeded in deriving an expression for the self-similar profile $\overline{c}_s$ of the mean concentration $\overline{c}$. This result is a step forward in our search for the value of $\mathcal{I}(\alpha,\gamma,\mathbf{p})$ that will eventually enable us to link α and γ. However, Eq. (32) alone is not sufficient to fulfill this objective. The reason is that, in Eq. (32), $\overline{c}_s$ is expressed as a function of the nondimensional variable z, and not of the variable y appearing in the definition (16b) of $\mathcal{I}$. With $y=z/(2F_0)$, this difference means that F_0 appears as an unknown parameter when combining Eqs. (32) and (16b). To overcome this issue and derive a closed expression for F_0, an additional assumption is required. The description of this hypothesis and of its consequences is the subject of this subsection.

1. Predominance of the growing mode

To begin with, let us recall that F_0 is the coefficient of the main order of the Legendre expansion (22) of the concentration flux $\overline{u_3'c'}$. Given our first approximation and the possibility to truncate this expansion, F_0 can also be recast as a function of the integral of $\overline{u_3'c'}$. Integrating Eq. (25) over y, we find that

$$F_0=\frac{6\langle\overline{u_3'c'}\rangle}{V_L}\quad\text{with}\quad\langle\cdot\rangle=\int\mathrm{d}y=\frac{1}{L}\int\mathrm{d}x_3. \tag{39}$$

So to find F_0, we need to evaluate the spatial average of the concentration flux $\langle\overline{u_3'c'}\rangle$.

In nonreactive Rayleigh-Taylor turbulence [12,17], this quantity is modeled by considering that the dynamics of the mixing zone at energetic scales is driven by buoyancy production. For reactive turbulence, we follow the same path. Even though reactions strongly modify the state of the mixture by creating pockets of light and heavy fluids, we assume that the growth of the mixing zone is determined by the way these pockets of pure fluids move relative to one another under the action of buoyancy forces. As already noted, this assumption is coherent with the self-similar scalings (5) of L and X_c which depend only on $\mathtt{A}_t g$ and t.

This phenomenological description about the role played by buoyancy production is translated in quantitative terms as follows. In Boussinesq Rayleigh-Taylor turbulence, whether reactive or not, buoyancy production takes the form of a linear system acting on $\boldsymbol{u}'$ and c'. Setting aside the spatial variations of $\partial_3\bar{c}$, this system possesses three homogenized eigenmodes, a_+, a_0, and a_-. Among these modes, only a_+ is associated with a positive eigenvalue and is consequently enhanced by buoyancy production. The other two are either inhibited (a_-) or neutral (a_0). In nonreactive Rayleigh-Taylor turbulence [12,17], this enhanced mode is found to be highly dominant over the other ones for large and energetic scales. Our assumption—the second major assumption of this work—is that it is also the case for reactive Rayleigh-Taylor turbulence. In particular, we assume that the variance of the enhanced mode is large compared to the correlations involving the other modes:

$$\langle\overline{a_+^2}\rangle \gg \langle\overline{a_p a_q}\rangle \quad \text{with} \quad p, q \in \{0, -\}. \tag{40}$$

2. Relation between F_0 and α

Now, the velocity and concentration fields $\boldsymbol{u}'$ and c' can be expressed as linear combinations of a_+, a_-, and a_0 in spectral space. This linear dependency extends to turbulent spectra and, from there, to second-order correlations. Following [12], we can write that

$$\frac{\langle\overline{u_3'c'}\rangle}{V_L} = M_{pq}\langle\overline{a_p a_q}\rangle \quad \text{and} \quad \langle\overline{c'^2}\rangle = N_{pq}\langle\overline{a_p a_q}\rangle, \tag{41}$$

where $p, q \in \{+, -, 0\}$ and where M_{pq} and N_{pq} are matrices which depend on α_{L} and on the angular properties of the spectra of the eigenmodes [12]. Using assumption (40) and retaining only the dominant term, we can then approximate these expressions by

$$\frac{\langle\overline{u_3'c'}\rangle}{V_L} = M_{++}\langle\overline{a_+^2}\rangle \quad \text{and} \quad \langle\overline{c'^2}\rangle = N_{++}\langle\overline{a_+^2}\rangle. \tag{42}$$

Combining these two equalities and using the relation $\langle\overline{c'^2}\rangle = (1 - \Theta)/6$, we thus find that

$$\frac{\langle\overline{u_3'c'}\rangle}{V_L} = \frac{1}{6}\frac{M_{++}}{N_{++}}(1 - \Theta). \tag{43}$$

In [12], the multiplicative factor in front of $1 - \Theta$ was determined and found to be equal to

$$\frac{M_{++}}{N_{++}} = \frac{d_{cc}}{\alpha_{\mathrm{L}} + \sqrt{4\alpha_{\mathrm{L}} + \alpha_{\mathrm{L}}^2}}, \tag{44}$$

where $d_{cc} \in [0, 1]$ is the exact same parameter as the one appearing in Eqs. (10) and (11). Let us recall that d_{cc} characterizes the directional anisotropy of the spectrum of a_+ and tells whether turbulent structures are flat or elongated.

Combining Eqs. (39), (43), and (44) we eventually arrive at the following expression for F_0:

$$F_0 = \frac{d_{cc}}{\alpha_{\mathrm{L}} + \sqrt{4\alpha_{\mathrm{L}} + \alpha_{\mathrm{L}}^2}}(1 - \Theta). \tag{45}$$

This expression assumes only the predominance of the growing mode and is not restricted to the self-similar regime of the flow. Whenever this regime is reached, we have $\alpha_{\mathrm{L}} \to \alpha$ and $\Theta \to 0$, so that

$$\text{Self-similar regime :} F_0 = \frac{d_{cc}}{\alpha + \sqrt{4\alpha + \alpha^2}}. \tag{46}$$

Note that Eq. (45) is valid for both reactive and nonreactive Rayleigh-Taylor turbulence. However, its asymptotic self-similar expression (46) differs in both cases because the limits of α and Θ are not the same.

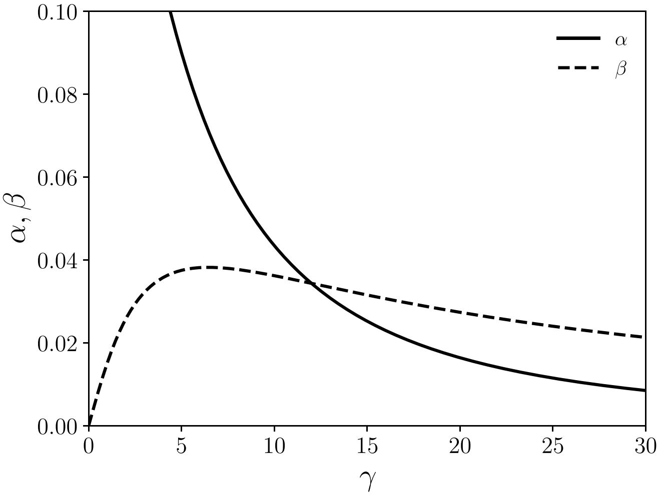

FIG. 5. Variations of α and β as a function of γ for $d_{cc} = 0.55$.

D. Main results

1. Asymptotic relation between α and γ

So far, we have derived an expression for the self-similar profile of $\bar{c}$ as well as an expression for the concentration flux prefactor F_0. With the help of these two intermediate results, we are now ready to express the integral $\mathcal{I}$ that serves as a basis for relating α and γ.

To start with, we make the change of variable $z = y/(2F_0)$ in the definition (16b) of $\mathcal{I}$ and inject the value (32) of $\bar{c}_\mathsf{s}$. This yields

$$\mathcal{I}(\alpha, \gamma, \mathbf{p}) = 12F_0 \int_{-1/2}^{1/2} \bar{c}_\mathsf{s}(z;\gamma)[1 - \bar{c}_\mathsf{s}(z;\gamma)]\,\mathrm{d}z. \tag{47}$$

Next, we replace the value of F_0 by its expression (46) and the value of the integral over z by the definition (36) of the length-scale ratio $\mathcal{G} = L/H$. With these substitutions, we are able to express $\mathcal{I}$ as

$$\mathcal{I}(\alpha, \gamma, \mathbf{p}) = \frac{2d_{cc}}{\alpha + \sqrt{4\alpha + \alpha^2}}\,\mathcal{G}(\gamma), \tag{48}$$

where $\mathcal{G}$ is the known function of γ given by Eq. (38) and shown in Fig. 4(b).

Thus, we have derived an expression for $\mathcal{I}$ that involves only α, γ and the same additional parameter d_{cc} that appears in the nonreactive relationships (10) and (11). All that remains to do is to solve Eq. (16a), i.e., $\mathcal{I} = 1$. This operation yields

$$\alpha = \frac{[d_{cc}\mathcal{G}(\gamma)]^2}{1 + d_{cc}\mathcal{G}(\gamma)}. \tag{49}$$

Because $\mathcal{G}$ is a decreasing function of γ, so is α. As shown in Fig. 5, the smaller γ is, the higher α is; and since small values of γ correspond to less mixing, the main conclusion that can be drawn from Eq. (49) is that the growth of the mixing zone is faster when the mixture is more heterogeneous. In other words, Eq. (49) confirms the intuitive link between growth rate and mixing that was mentioned in the introduction and that served as the main motivation for this work.

Another point worth mentioning is that α also depends on the anisotropy factor d_{cc} and increases with it. So, just as in nonreactive Rayleigh-Taylor turbulence, elongated structures are associated with a faster growth of the mixing zone.

2. Dynamic relation between $\alpha_{\rm L}$, $\gamma_{\rm L}$ and Θ

Figure 3 shows an important feature of reactive Rayleigh-Taylor flows: the nearly horizontal line observed in the $(\alpha_{\rm L}, \Theta)$ graph indicates that the convergence of Θ towards its zero asymptotic value is much slower than the convergence of $\alpha_{\rm L}$ towards α. Therefore, rather than a strict asymptotic state where Θ is equal to 0, it may be useful to account for an intermediate state where Θ is small but different from 0.

In this regard, most of the results derived so far can be used to analyze this intermediate state. In particular, the value of F_0 given by Eq. (45) does not depend on whether the asymptotic regime is reached or not. It remains valid even with nonzero values of Θ. The same remark applies to the truncation of the Legendre polynomial expansion of Sec. III B and by extension to Eq. (28). The only question that we need to answer is how a finite value of Θ affects the self-similar profile $\overline{c}_{\rm s}$ deduced from Eq. (28). Without further constraints to guide us, we propose to settle for the simplest possible solution. Namely, we assume that $z(t, c)$ and F_0 remain stationary so that Eq. (30) still applies. Then $\overline{c}_{\rm s}$ keeps its expression (32), save for one modification: the asymptotic parameter γ in Eq. (32) must be replaced by the instantaneous value of the parameter appearing in Eq. (28) as a prefactor of $c(1 - c)$, i.e., by $\gamma_{\rm L}$, the dynamic estimate of γ introduced in Eq. (6). Thus, replacing Eq. (46) by Eq. (45) and γ by $\gamma_{\rm L}$, we deduce the following dynamic estimate of $\alpha_{\rm L}$:

$$\alpha_{\rm L} = \frac{[d_{cc}(1-\Theta)\mathcal{G}(\gamma_{\rm L})]^2}{1 + d_{cc}(1-\Theta)\mathcal{G}(\gamma_{\rm L})}. \tag{50}$$

The most striking property of Eq. (50) is that, even though it was derived in a reactive setting, its validity extends to nonreactive Rayleigh-Taylor flows. Indeed, the absence of reaction corresponds to the limit $\tau \to \infty$ and therefore to $\gamma_{\rm L} = 0$. As a result, since $\mathcal{G}(0) = 1$, we find that

$$\text{for} \quad \tau \to \infty, \quad \alpha_{\rm L} = \frac{[d_{cc}(1-\Theta)]^2}{1 + d_{cc}(1-\Theta)}. \tag{51}$$

This formula is identical to Eq. (10) which was derived in [11,12] for nonreactive Rayleigh-Taylor turbulence. Let us also mention that with $\gamma_{\rm L} = 0$, the profile $\overline{c}_{\rm s}(z, \gamma_{\rm L})$ given by Eq. (32) is linear, just like was assumed in [11,12]. Thus, the reactive/nonreactive coincidence in the limit $\tau \to \infty$ applies not only to the end result [Eq. (50)] but also to the main assumptions that lead to it.

3. Displacement rate β

At the beginning of the derivation, in Sec. III A 1, we explained how the integration of Eq. (12) leads to Eq. (14), i.e., to $\beta = \gamma\alpha/12$. Combining this relation with the expression (49) of α yields the following expression of β:

$$\beta = \frac{\gamma}{12}\frac{[d_{cc}\mathcal{G}(\gamma)]^2}{1 + d_{cc}\mathcal{G}(\gamma)}. \tag{52}$$

The most salient feature of this expression is that β is not a monotonic function of γ. It is equal to 0 for $\gamma = 0$ and decays as $3d_{cc}^2/\gamma$ for large γ. Between the two limits, β goes through a maximum. For d_{cc} on the order of 1, this maximum is reached for $\gamma = \gamma_{\max} \approx 6$ and its value verifies

$$\beta_{\max} \approx \frac{d_{cc}}{12}\left(d_{cc} + \frac{3}{10}\right). \tag{53}$$

For $d_{cc} = 0.55$, a value observed in the simulation detailed in Sec. IV, we find that $\beta_{\max} \approx 0.04$, a value obtained for $\gamma_{\max} \approx 6.5$. These properties are illustrated in Fig. 5.

From a physical point of view, the reason why β attains a maximum can be understood as follows. The quantity $X_c = \int (\overline{c} - \overline{c}^{(0)})\,{\rm d}x_3$ not only traces the displacement of the center of the mixing zone. It also corresponds to the total volume of reactant which has been burnt since initial time. Hence, β can also be seen as a measure of the increase of the consumption rate of reactants by the mixing zone. As shown by Eq. (13), this consumption rate is proportional to two factors. The first one is the width of the flame brush [L in Eq. (13)], the other the proportion of burning fluids found within this brush [Θ in Eq. (13)]. These two factors vary in opposite directions with the level of mixing γ: L is proportional to α and decreases with γ, while, by definition, Θ increases with γ.

To sum up, the dependency of β on the mixing level γ is controlled by two factors with opposing effects. The maximum predicted by Eq. (52) corresponds to the optimal consumption rate that can be achieved under these antagonizing conditions. Given the double interpretation of X_c, this maximum also corresponds to the largest acceleration that the center of the mixing zone can achieve. The fact that such a maximal value exists may be of importance for some applications. For instance, the transition from deflagration to detonation of Rayleigh-Taylor driven flames in type Ia supernovae is possibly influenced by the speed at which these flames travel [31].

To conclude on the displacement rate, we have hitherto discussed its asymptotic value β. A dynamic estimate β_{L} of this coefficient was introduced in Eq. (6), based on the same time scale τ_L as the one appearing in the definitions of α_{L} and γ_{L}. Because of this choice, Eq. (13) can be written in a strictly equivalent form linking α_{L}, β_{L}, and γ_{L}:

$$\beta_{\mathrm{L}} = \frac{\gamma_{\mathrm{L}}}{12}\alpha_{\mathrm{L}} = \frac{\gamma_{\mathrm{L}}}{12}\frac{[d_{cc}(1-\Theta)\mathcal{G}(\gamma_{\mathrm{L}})]^2}{1+d_{cc}(1-\Theta)\mathcal{G}(\gamma_{\mathrm{L}})}. \tag{54}$$

Just as Eq. (50) for α_{L}, this prediction is valid in both reactive and nonreactive turbulence. In the latter case, we recover the trivial result:

$$\text{for} \quad \tau \to \infty, \quad \beta_{\mathrm{L}} = 0. \tag{55}$$

IV. SIMULATIONS

A. Simulation setting and initial conditions

In order to verify the validity of the results derived in the previous section, four direct numerical simulations (DNS) and four implicit large eddy simulations (ILES) are carried out. The reason for performing ILES in addition to DNS is that the former allows us to attain higher effective Reynolds numbers. This gives more leeway for exploring the thickened-wrinkled flame regime (see Fig. 2) and for attaining a state close to self-similarity. Another reason is that we are mostly interested in the evolution of the large-scale features of the flows and do not need a detailed knowledge on the evolution of small dissipative scales. These scales are of course captured by DNS. Thus, the comparison between the two approaches allows us to verify that the role played by these scales is not crucial for the issues at stake in this work and that no physical bias is introduced by using a numerical dissipation instead of a physical one.

The DNS and ILES are performed with two different codes. The DNS are done with STRATOSPEC, which is a spectral code solving the reactive Boussinesq equations (1). The computationnal grid is a rectangular domain with regular spacing and dimensions $L_{\mathrm{dom}} \times L_{\mathrm{dom}} \times 2L_{\mathrm{dom}}$ with $L_{\mathrm{dom}} = 2\pi$. The simulations all have $2048^2 \times 4096$ cells [37].

The ILES are performed with TRICLADE, which is a finite-volume solver of the compressible multimaterial Navier–Stokes equation [38,39]. The computational grid is subdivided in three adjacent domains. The central domain is regular and has $1024^2 \times 1280$ cells. Its dimensions are $L_{\mathrm{dom}} \times L_{\mathrm{dom}} \times 1.25L_{\mathrm{dom}}$ with $L_{\mathrm{dom}} = 1$. The other domains have a geometric progression in the inhomogeneous direction. Note that, even if the code is compressible, the simulations remains in the Boussinesq limit. The Atwood number at the interface is small ($\mathtt{A}_t = 0.025$) and the turbulent Mach number also remains small at all times.

For both types of simulation, a random perturbation h corrugates the interface between the two fluids. The prescribed spectrum for the perturbation takes the form

$$P(k) = \overline{h^2}\,\frac{2\left(\frac{s}{2}\right)^{\frac{s+1}{2}}}{\Gamma\left(\frac{s+1}{2}\right)}\frac{\lambda_0}{2\pi}\left(\frac{k\lambda_0}{2\pi}\right)^{s} e^{-\frac{s}{2}\left(\frac{k\lambda_0}{2\pi}\right)^2}, \tag{56}$$

TABLE I. Initial Damköhler number $\mathtt{Da}_0$ of simulations.

	DNS					LES			
Simulation name	NR	D1	D2	D3	D4	L1	L2	L3	L4
$\mathtt{Da}_0$	0	0.8	1.6	2.5	3.3	1.0	1.6	2.1	2.6

where $\overline{h^2}$ is the variance of the perturbation height, λ_0 the peak length scale of the perturbation spectrum, and s the infrared exponent of the spectrum. The following parameters are set for the simulations:

$$\text{DNS:} \quad s = 6, \quad \frac{\lambda_0}{L_{\text{dom}}} = 2.5 \times 10^{-2}, \quad \frac{\sqrt{\overline{h^2}}}{L_{\text{dom}}} = 1.3 \times 10^{-3},$$

$$\text{LES:} \quad s = 6, \quad \frac{\lambda_0}{L_{\text{dom}}} = 6 \times 10^{-3}, \quad \frac{\sqrt{\overline{h^2}}}{L_{\text{dom}}} = 3 \times 10^{-3}.$$

The typical time of growth associated with this perturbation spectrum is given by

$$T_{\text{RT}} = \sqrt{\frac{\lambda_0}{2\pi \mathtt{A}_t g}}, \tag{57}$$

This time can be compared against the reactive timescale τ, thus leading to the definition of a dimensionless parameter called the initial Damköhler number $\mathtt{Da}_0$:

$$\mathtt{Da}_0 = \frac{T_{\text{RT}}}{\tau} = \sqrt{\frac{\lambda_0}{2\pi \mathtt{A}_t g \tau^2}}. \tag{58}$$

For each simulation, the initial Damköhler number is modified by changing the reaction timescale τ while keeping other parameters unchanged. The value of $\mathtt{Da}_0$ for each simulation is given in Table I.

The initial Damköhler number $\mathtt{Da}_0$ is not expected to play a significant role in the self-similar regime. However, $\mathtt{Da}_0$ plays a crucial role during the transient evolution of the flow. In particular, the value of $\mathtt{Da}_0$ is the main factor that determines the delay after which the thickened-wrinkled flame regime and the self-similar regime can be reached. In this respect, two limits can be put forward. If $\mathtt{Da}_0 \gg 1$, the reaction is much faster than the Rayleigh-Taylor instability. The laminar flame front is corrugated by the Rayleigh-Taylor instability and transitions from a flamelet to a thickened-wrinkled flame. On the other hand, when $\mathtt{Da}_0 \ll 1$, the reaction is very slow compared to the Rayleigh-Taylor instability. As a consequence, there may be a significant time during which the reaction does not affect the evolution of the mixing zone. In that case, the flow goes transiently through the thickened flame regime before reaching the thickened-wrinkled flame regime. Examples of these different transients can be observed in Fig. 2.

Note that simulation NR has a Damköhler number equal to 0: the reaction time is infinite so that the simulation is nonreactive. This simulation is used as a reference against which the remaining reactive simulations can be compared.

B. Flow characteristics

The main predictions of this work concern three quantities: the width of the mixing zone L, the displacement of its center X_c, and the mixing parameter Θ [see Eq. (4)]. Figure 6 illustrates how these three quantities behave for the DNS D2 ($\mathtt{Da}_0 = 1.6$) and the LES L3 ($\mathtt{Da}_0 = 2.1$). As a reference, the nonreactive simulation NR ($\mathtt{Da}_0 = 0$) is also plotted in this figure. As can be seen, after a short transient, the width L and displacement X_c grow almost quadratically in time for both reactive simulations, while the mixing parameter decays almost as the inverse of time. This

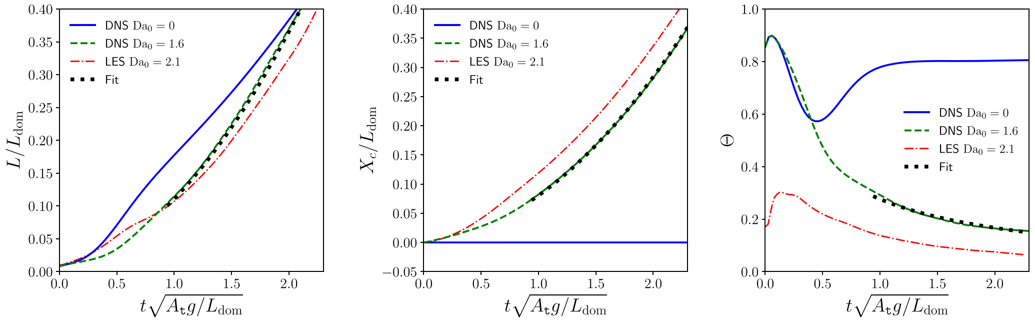

(a) Mixing zone width

(b) Displacement of the center

(c) Mixing parameter

FIG. 6. Mixing zone width L, flame displacement X_c and mixing parameter for simulations NR ($\mathtt{Da}_0 = 0$), D2 ($\mathtt{Da}_0 = 1.6$), and L3 ($\mathtt{Da}_0 = 2.1$). The fitted values are defined by Eq. (59) with parameters given by Eq. (60).

is confirmed by comparing their evolution with fits of the form

$$L_{\mathrm{fit}}(t) = [\sqrt{2\alpha_{\mathrm{fit}}\mathtt{A}_t g}(t - t_s) + \sqrt{L(t_s)}]^2, \quad X_{c,\mathrm{fit}}(t) = [\sqrt{2\beta_{\mathrm{fit}}\mathtt{A}_t g}(t - t_s) + \sqrt{X_c(t_s)}]^2, \tag{59}$$

$$\text{and} \quad \Theta_{\mathrm{fit}}(t) = \frac{\gamma_{\mathrm{fit}}\tau}{t - t_s + \gamma_{\mathrm{fit}}\tau/\Theta(t_s)},$$

where α_{fit}, β_{fit} and γ_{fit} are adjustable parameters and where t_s is a time marking the onset of self-similarity. Choosing $t_s\sqrt{\mathtt{A}_t g/L_{\mathrm{dom}}} = 1$, a best fit of the DNS with $\mathtt{Da}_0 = 1.6$ is obtained by setting

$$\alpha_{\mathrm{fit}} \approx 0.037, \quad \beta_{\mathrm{fit}} \approx 0.031, \quad \text{and} \quad \gamma_{\mathrm{fit}} \approx 11. \tag{60}$$

With these values, a close agreement is observed between the actual and fitted evolutions of L, X_c, and Θ. This is consistent with the expected self-similar behavior predicted in Eq. (5). While not shown here, a similar agreement is obtained for the LES with $\mathtt{Da}_0 = 2.1$, as well as for the remaining reactive reactions, with values of α_{fit}, β_{fit}, and γ_{fit} close to those given here.

It is worth stressing that the value $\gamma_{\mathrm{fit}} \approx 11$, when reported in Eq. (49) and Fig. 5, leads to values of α and β close to the fitted ones. This coherency gives a first hint as to the validity of Eq. (49). It should also be emphasized that the estimate α_{fit} is larger than the value $\alpha_{\mathrm{nr}} = 0.02$ usually measured in nonreacting Rayleigh-Taylor simulations [4,5,7]. This property will be confirmed below by looking at the time evolution of α_{L} (see Fig. 12). Note also that the quadratic time evolution of L appears more clearly for the two reactive cases than the nonreactive one in Fig. 6(a). For the latter, a longer transient is present. Figure 6(c) also shows that in the nonreactive case, Θ tends to a constant approximately equal to 0.8. As mentioned in the introduction and in Sec. II C, this is one of the major differences distinguishing reactive and nonreactive Rayleigh-Taylor turbulence.

This major difference is also illustrated in Fig. 7, which displays vertical cuts of the concentration and vorticity fields for the reactive DNS D2 ($\mathtt{Da}_0 = 1.6$) and the nonreactive DNS NR ($\mathtt{Da}_0 = 0$) at a time such that $L/L_{\mathrm{dom}} = 0.7$. The concentration field displayed for the reactive simulation shows a domain mostly filled by pure fluids: the red and blue colors are predominant. By contrast, the nonreactive cut essentially shows intermediate colors within the mixing zone suggesting a high level of mixing.

Figure 7 also shows another property of reactive Rayleigh-Taylor turbulence worth mentioning. First, looking at the two cuts on the left of this figure, one can see that, in the Boussinesq limit, a nonreactive Rayleigh-Taylor mixing zone develops symmetrically with respect to the position of the initial interface separating the two fluids. Also, the extent of the vorticity field roughly coincides with that of the concentration field. By contrast, the concentration and vorticity fields of the reactive case are highly asymmetrical: with respect to the layer center, their extension is greater in the direction of light products than in the direction of heavy reactants. Furthermore, one can note that

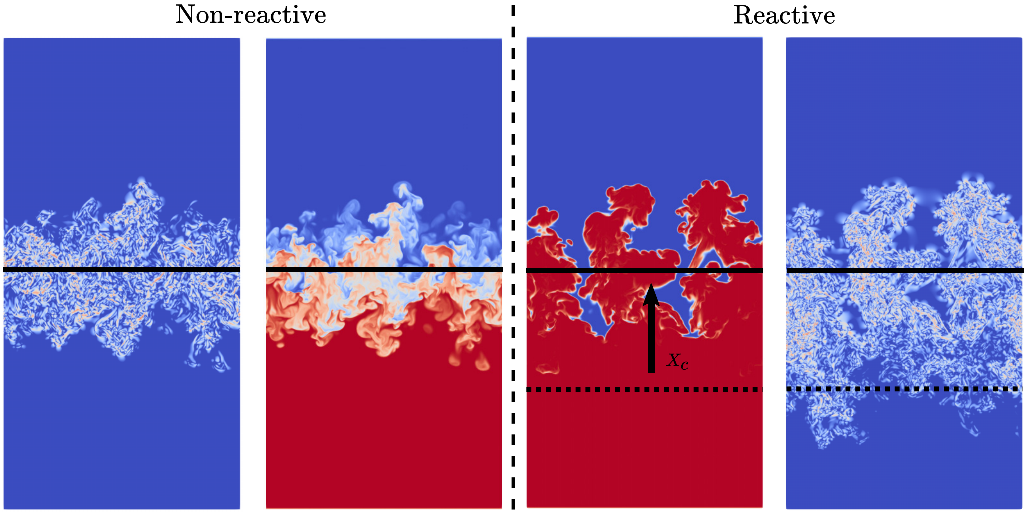

FIG. 7. Vertical slices of the concentration field and of the longitudinal vorticity magnitude $\log \omega_x^2$ for the reactive DNS D2 ($\mathtt{Da}_0 = 1.6$) and the nonreactive DNS NR ($\mathtt{Da}_0 = 0$) at a time such that $L/L_{\text{dom}} = 0.7$. The nonreactive DNS is shown in the left-half and the reactive DNS in the right-half of the figure. In each half, vorticity is shown in the outer panel and concentration in the inner one. For the concentration field, red corresponds to $c = 1$ (light products) and blue to $c = 0$ (heavy reactants). For the vorticity field, a brighter color means a higher intensity.

the vorticity field extends below the mixing region down to the position of the initial interface and even somewhat below. To understand the origin of this observation, the interplay between vorticity production and flame displacement has to be considered. At any time, the flame is the locus of the strongest concentration gradients and hence of the strongest density gradients in the present Boussinesq flow. Due to the baroclinic torque, it means that most of the instantaneous vorticity production occurs inside the reacting zone. Then the deposited vorticity remains attached to the fluid, and more precisely to the products, whereas the flame propagates toward the reactants. This is different from the nonreacting case, where density gradients and vorticity are both carried by the fluid, leading to persistent amplification at the same place. By contrast, in the reacting case, the vorticity deposited at any time at the instantaneous flame location decays later in the light products, whereas the baroclinic production zone propagates upward toward the reactants. Would no vortex dynamics be at work, the vorticity field would be confined between the initial and the final position of the flame front. In the right half of Fig. 7, it would correspond to the red region of products above the dashed line. However, this trailing field is not passive, and turbulent motions may entrain some fluid with its vortical content below the initial flame location as seen in Fig. 7. This is also seen in Fig. 1, which shows a volume rendering of the concentration field.

C. Verification of the assumptions

To derive the results presented in Sec. III D, we made two major assumptions. First, we assumed that the flux and variance of the concentration can be approximated by a truncated Legendre approximation. Second, we assumed that the growing mode of the buoyancy production term is large compared to the other ones and is dominant in the expressions of the concentration flux and variance. The relevance of these two assumptions is assessed below.

We also check whether the anisotropy coefficient d_{cc} remains constant and close to the same value in the different simulations. This condition is not a requirement for the derivation of Eqs. (49)– (50)

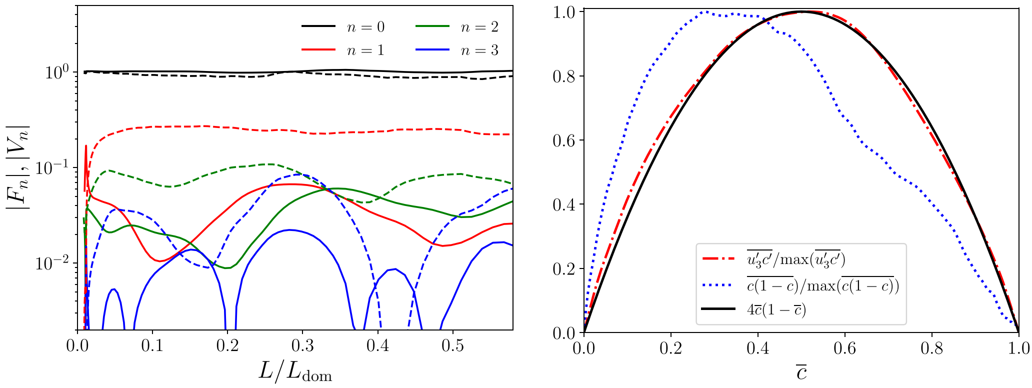

(a)

(b)

FIG. 8. Dependency of the spatial profiles of $\overline{u_3'c'}$ and $\overline{c(1-c)}$ on the mean concentration $\bar{c}$. Results taken from simulation D4, at the time for which $L/L_{\mathrm{dom}} = 0.2$ for (b). (a) Legendre polynomial coefficients F_n (solid lines) and V_n (dashed lines) of $\overline{u_3'c'}$ and $\overline{c(1-c)}$ [Eq. (22)]. (b) Correlations $\overline{u_3'c'}$ and $\overline{c(1-c)}$ normalized by their maxima as a function of the mean concentration $\bar{c}$.

and (52)– (54). However, if it is not verified, d_{cc} cannot be regarded as a fixed parameter, and some additional considerations would be needed to make full sense of Eqs. (49)–(50) and (52)– (54).

1. *Spatial profiles of the flux and variance of concentration*

The first pivotal hypothesis made in this work is expressed by Eq. (25). It consists in assuming that the correlations $\overline{u_3'c'}$ and $\overline{c(1-c)} = \bar{c}(1-\bar{c}) - \overline{c'^2}$ are proportional to $\bar{c}(1-\bar{c})$ and to a time-dependent constant. This assumption can be understood as the result of the truncation of the Legendre polynomial expansion (22) and may be justified provided the higher-order coefficients of this expansion are much smaller than its zeroth order [Eq. (24)].

To verify these elements, we plot in Fig. 8(a) the first three Legendre polynomial coefficients of $\overline{u_3'c'}$ and $\overline{c(1-c)}$ for simulation D4 as a function of time. These coefficients are computed according to the formulas

$$F_n(t) = \int_0^1 \frac{\overline{u_3'c'}}{4\max(\overline{u_3'c'})}\bar{c}(1-\bar{c})\tilde{P}_n(\bar{c})d\bar{c} \quad \text{and} \quad V_n(t) = \int_0^1 \frac{\overline{c(1-c)}}{4\max[\overline{c(1-c)}]}\bar{c}(1-\bar{c})\tilde{P}_n(\bar{c})d\bar{c}. \tag{61}$$

The first observation is that F_0 and V_0 are indeed much larger than their respective higher order coefficients F_i and V_i with $i \in \{1, 2, 3\}$. This is coherent with Eq. (24) and with the possibility of truncating expansion (22). A second observation worth mentioning is that the first three coefficients of the expansion vary little in time. This implies that almost from the start of the simulation, way before the self-similar turbulent regime has begun, the profiles of $\overline{u_3'c'}$ and $\overline{c(1-c)}$ expressed as a function of $\bar{c}$ have already almost settled to their asymptotic shapes. The larger fluctuations observed for F_3 and V_3 might be assigned to the statistical fluctuations that inevitably deform correlation profiles.

To provide a more direct verification of Eq. (25), we display in Fig. 8(b) the correlations $\overline{u_3'c'}$ and $\overline{c(1-c)}$ normalized by their maxima as a function of $\bar{c}$. These profiles are shown for simulation D4 at the time for which $L/L_{\mathrm{dom}} = 0.2$. For $\overline{u_3'c'}$, a close agreement is observed with the parabola $4\bar{c}(1-\bar{c})$, as expected from Eq. (25). However, for $\overline{c(1-c)}$, a non-negligible asymmetry of the normalized shape is observed. Its peak is indeed reached for $\bar{c} \approx 0.35$ instead of 0.5. This asymmetry comes from the coefficient V_1 of the Legendre expansion, and, even though it appears significant, its effects

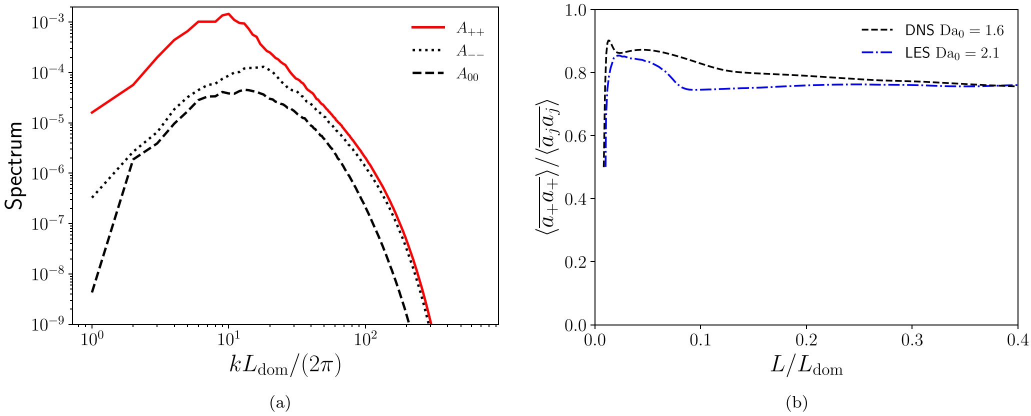

FIG. 9. Illustration of the predominance of the growing eigenmode. (a) Spectra of the homogeneous eigenmodes a_+, a_-, and a_0 for simulation D4 at a time such that $L/L_{\rm dom} = 0.14$. (b) Relative contribution of the growing eigenmode a_+ to the total energy for simulations D2 and L3.

on the results presented so far are not. To check it, the derivation of Sec. III has been performed again keeping the contribution of V_1. While this modified derivation is not detailed here, we found no important changes to the self-similar concentration profile $\overline{c}_{\rm s}$ nor to the eventual dependency of α and β on γ, provided V_1/V_0 remains small as is the case in our simulations. In particular, with the ratio V_1/V_0 displayed in Fig. 8(a), the formula accounting for V_0 and V_1 differs only by a few percent from Eqs. (49) and (52), which account only for V_0.

Thus, as whole, the results displayed in Figs. 8(a) and 8(b) appear compatible with the assumption given in Sec. III B.

2. *Predominance of the growing mode*

The second major hypothesis of this work is described in Sec. III C and consists in assuming that, among the three eigenmodes of the homogenized linear buoyancy production term, the growing one, a_+, is much larger than the other two, a_- and a_0. This condition is expressed by Eq. (40).

To verify this assumption, we begin by comparing the three-dimensional spectra A_{++}, A_{00}, and A_{--} of each of these modes. Figure 9(a) shows this comparison for simulation D4 at a time such that $L/L_{\rm dom} = 0.14$. It can be seen that A_{++} is indeed much larger than A_{00} and A_{--} at large and energetic scales. A more direct verification of Eq. (40) is obtained by plotting the ratio $\langle\overline{a_+^2}\rangle/\langle\overline{a_ja_j}\rangle$ as a function of time. This is done in Fig. 9(b) for simulations D2 and L3. It can be seen that $\langle\overline{a_+^2}\rangle$ throughout the simulations represents more than 75% of the sum $\langle\overline{a_ja_j}\rangle$ which measures the total energy, i.e., the sum of the kinetic and potential energies. Overall, the results displayed in Figs. 9(a) and 9(b) are consistent with assumption (40).

3. *Anisotropy parameter d_{cc}*

Even though it is not required for their derivations, we still interpreted and manipulated relations (49)–(50) and (52)–(54) with the implicit expectation that d_{cc} attains a constant value independent from initial conditions. Otherwise, relations (49)– (50) and (52)–(54) would still be valid but unknown dependencies would remain hidden in the value of d_{cc}. To verify that this is not the case, we invert relation (45) and express d_{cc} as

$$d_{cc} = \frac{F_0}{1-\Theta}\left(\alpha_{\rm L} + \sqrt{4\alpha_{\rm L} + \alpha_{\rm L}^2}\right). \tag{62}$$

This expression is plotted as function of time for the DNS and LES simulations in Fig. 10. It can be seen that d_{cc} indeed reaches a constant value and that this value varies by less than 10% in the

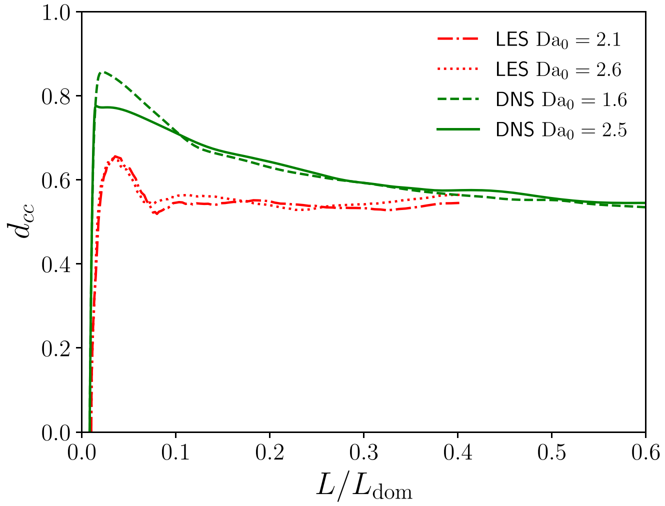

FIG. 10. Evolution of d_{cc} given by formula (62) as a function of $L/L_{\rm dom}$ for the DNS and LES simulations.

different simulations. More precisely, we observe that for $L/L_{\rm dom} > 0.2$, we have

$$d_{cc} \approx 0.55 \pm 10\%. \tag{63}$$

D. Main predictions

1. *Mean concentration profile*

Assumptions (25) and (40) lead to several predictions and in particular to the derivation of the analytic formula (32) giving the mean concentration profile as a function of the reduced coordinate $z = x_3/(2F_0L)$. This expression is valid at asymptotically large times. However, for the simulations performed in this work, the transient preceding the self-similar regime induces an offset of the profiles that survives until the simulations end. This offset prevents a direct comparison of Eq. (32) with simulation results.

To circumvent this difficulty, we propose to account for the transient part of the simulation in the expression of z. Namely, in the preceding subsection, we observed in Figs. 8(a) and 9(b) that assumptions (25) and (40) are valid almost from the start of the simulations. This means that the unstationary equation (28) giving the evolution of z as a function of time and $\overline{c}$ is also valid at these early times. As a result, the transient evolution of z can be computed from Eq. (28). This can be done by using the method of characteristics, assuming that the viscous terms are negligible. This yields

$$z(t^*, \overline{c}) = z_{\rm off}(t^*, \overline{c}) + C_z(t^*) z_{\rm cent}(t^*, \overline{c}) \tag{64a}$$

$$\text{with } z_{\rm off}(t^*, \overline{c}) = z_{\rm init}\left(\frac{\overline{c}e^{-\Delta\Gamma(0,t^*)/2}}{1 - c + ce^{-\Delta\Gamma(0,t^*)/2}}\right)\frac{F_{0,\rm init}}{F_0(t^*)}e^{-t^*}, \tag{64b}$$

$$z_{\rm cent}(t^*, \overline{c}) = -\frac{1}{2C_z(t^*)}\int_0^{t^*} e^{-(t^*-s)}\frac{F_0(s)}{F_0(t^*)}\frac{\overline{c}e^{-\Delta\Gamma(s,t^*)/2} - (1-\overline{c})}{\overline{c}e^{-\Delta\Gamma(s,t^*)/2} + (1-\overline{c})}\,\mathrm{d}s, \tag{64c}$$

$$C_z(t^*) = \int_0^{t^*} e^{-(t^*-s)}\frac{F_0(s)}{F_0(t^*)}\,\mathrm{d}s, \tag{64d}$$

$$\text{and } t^* = \int_0^t \frac{\mathrm{d}t'}{\tau_L(t')}, \quad \Delta\Gamma(s, t^*) = \int_s^{t^*} \gamma_{\rm L}(t')\,\mathrm{d}t'. \tag{64e}$$

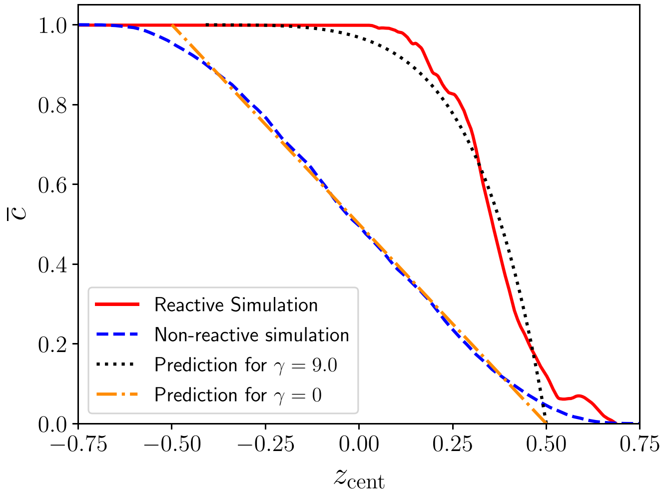

FIG. 11. Mean concentration profile as a function of the reduced coordinate z_{cent} [Eq. (64)]. Comparison between the reactive DNS D3, the nonreactive DNS NR, and the analytical prediction (32) at a time such that $L/L_{\mathrm{dom}} = 0.4$. For the nonreactive prediction, the value $\gamma = 0$ is used in Eq. (32), and for the reactive one, the value $\gamma = 9$ measured in the simulation is used.

The different terms of these expressions can be computed using the values of F_0 and γ_{L} extracted from the simulations. This allows us to separate the contribution of the offset due to the initial condition, z_{off}, from the contribution converging to the self-similar solution (31) in a symmetric fashion at large times, z_{cent}.

Figure 11 shows the value of $\overline{c}$ as a function of z_{cent} for simulation D3 at a time for which $L/L_{\mathrm{dom}} = 0.4$. This simulation result is compared against the expression of $\overline{c}_{\mathrm{s}}$ given by Eq. (32) with $\gamma = 9$ set to the measured value of γ_{L} at $L/L_{\mathrm{dom}} = 0.4$. A good agreement is observed between prediction and simulation. The most salient difference is observed at the foot of the concentration profile. In the simulation, a small overshoot extends beyond the limit $z = 0.5$, which is not predicted by Eq. (32). Similar observations are made at different times and also for the other simulations, whether they are DNS or LES.

To insist on the difference between the reactive and nonreactive cases, we also plotted in Fig. 11 the profile obtained for the nonreactive Rayleigh-Taylor simulation NR. It can be seen that the nonreactive profile remains mostly symmetric and varies almost linearly for $z_{\mathrm{cent}} \in [-0.5, 0.5]$. By contrast, the reactive profile is highly asymmetric and varies rapidly close to $z_{\mathrm{cent}} = 0.5$. Note that deviations from linearity appear close to the edges of the nonreactive zone.

2. Growth and displacement rates, α and β

In Sec. III D we derived formulas relating the asymptotic parameters α, β, and γ as well as formulas relating instantaneous estimates of these parameters denoted by α_{L}, β_{L}, and γ_{L}. In simulations, only the latter quantities can be extracted so that the main predictions that can be checked are Eqs. (50) and (54).

A first way of assessing these predictions is by injecting into the right-hand side of Eqs. (50) and (54) the instantaneous values of d_{cc}, Θ, and γ_{L} computed in the simulations and by comparing the outcome against the values of α_{L} and β_{L}, also computed in the simulations by using their definitions (6). This comparison is shown in Fig. 12 for simulations D2 and L4. A good agreement is obtained between simulation and prediction. This agreement occurs early in the simulation, before the onset of the self-similar regime. This is coherent with the previous observations according to which assumptions (25) and (40) are verified at early times [see Fig. 8(a) and 9]. Similar outcomes are observed for the remaining simulations. Another way of verifying Eqs. (50) and (54) is by focusing

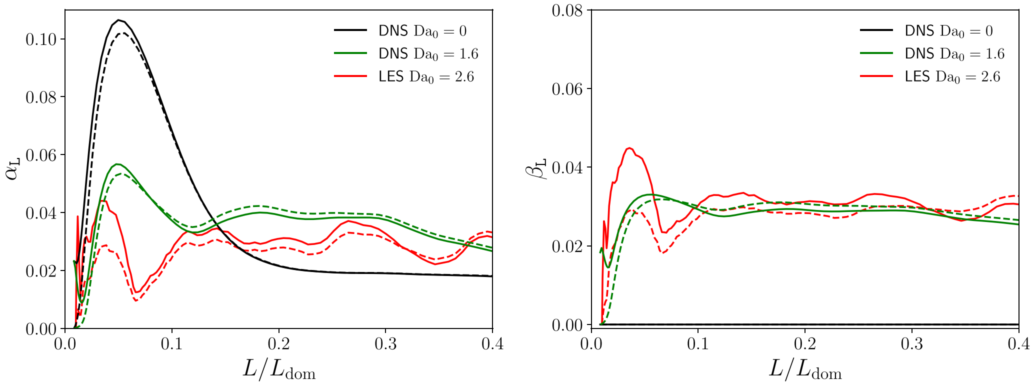

(a) $\alpha_{\rm L}$ as a function of time.

(b) $\beta_{\rm L}$ as a function of time.

FIG. 12. Time evolution of $\alpha_{\rm L}$ and $\beta_{\rm L}$ for simulations D2 and L4. Comparison between the instantaneous estimates of $\alpha_{\rm L}$ and $\beta_{\rm L}$ (Eq. (6)) and their theoretical predictions [Eqs. (50) and (54)]. Plain lines: simulations; dashed lines: predictions.

on the late times of the simulations, when the flow is close to its self-similar state and still far from being confined. This "self-similar" interval of time is observed when $0.1 < L/L_{\rm dom} < 0.4$ for LES and when $0.2 < L/L_{\rm dom} < 0.4$ for DNS. For these intervals of time, d_{cc} is approximately constant and equal to its asymptotic value of 0.55 [see Fig. 10 and Eq. (63)]. Then Eqs. (50) and (54) can be assessed by enforcing this constant value in their right-hand sides.

However, even with this specification, Eqs. (50) and (54) remain hybrid relations that combine two different metrics of the mixing level: Θ and $\gamma_{\rm L}$. Even though Θ tends to 0, its influence lingers. To cast this influence aside and isolate the dependency on $\gamma_{\rm L}$, we therefore propose to introduce the following modified values of $\alpha_{\rm L}$ and $\beta_{\rm L}$:

$$\alpha_{\rm L}^\star = \frac{[s_\alpha/(1-\Theta)]^2}{1+s_\alpha/(1-\Theta)} \quad \text{and} \quad \beta_{\rm L}^\star = \frac{[s_\beta/(1-\Theta)]^2}{\gamma_{\rm L}/12 + s_\beta/(1-\Theta)} \tag{65}$$

$$\text{with} \quad s_\alpha = \frac{\alpha_{\rm L} + \sqrt{4\alpha_{\rm L} + \alpha_{\rm L}^2}}{2} \quad \text{and} \quad s_\beta = \frac{\beta_{\rm L} + \sqrt{\gamma_{\rm L}\beta_{\rm L}/3 + \beta_{\rm L}^2}}{2}.$$

When $\Theta = 0$, one has $\alpha_{\rm L}^\star = \alpha_{\rm L}$ and $\beta_{\rm L}^\star = \beta_{\rm L}$ so that the two sets of quantities carry the same asymptotic information. However, they differ at intermediate times when $\Theta \neq 0$. The interest of defining $\alpha_{\rm L}^\star$ and $\beta_{\rm L}^\star$ is the following. Injecting Eqs. (50) and (54) into these expressions, we find the following prediction for the values of $\alpha_{\rm L}^\star$ and $\beta_{\rm L}^\star$:

$$\alpha_{\rm L}^\star = \frac{[d_{cc}\mathcal{G}(\gamma_{\rm L})]^2}{1 + d_{cc}\mathcal{G}(\gamma_{\rm L})} \quad \text{and} \quad \beta_{\rm L}^\star = \frac{\gamma_{\rm L}}{12}\frac{[d_{cc}\mathcal{G}(\gamma_{\rm L})]^2}{1 + d_{cc}\mathcal{G}(\gamma_{\rm L})}. \tag{66}$$

Thus, even when $\Theta \neq 0$, the predicted values of $\alpha_{\rm L}^\star$ and $\beta_{\rm L}^\star$ depend only on $\gamma_{\rm L}$. These predicted values can thus be compared more easily against simulation results.

This comparison is shown in Fig. 13. Simulation results are displayed for the "self-similar" interval of time mentioned above and correspond to a direct evaluation of $\alpha_{\rm L}^\star$ and $\beta_{\rm L}^\star$ as given by Eq. (65). The theoretical curve shown as a black line corresponds to Eq. (66) with $d_{cc} = 0.55$. As can be seen, the simulation points align along the theoretical curve for values of $\gamma_{\rm L}$ ranging from 8 to 20, the largest differences being on the order of 15%. It is worth highlighting that, for this range of $\gamma_{\rm L}$, $\alpha_{\rm L}^\star$ has ample variations spreading in between 0.015 and 0.06. By contrast, $\beta_{\rm L}^\star$ varies only between 0.027 and 0.042.

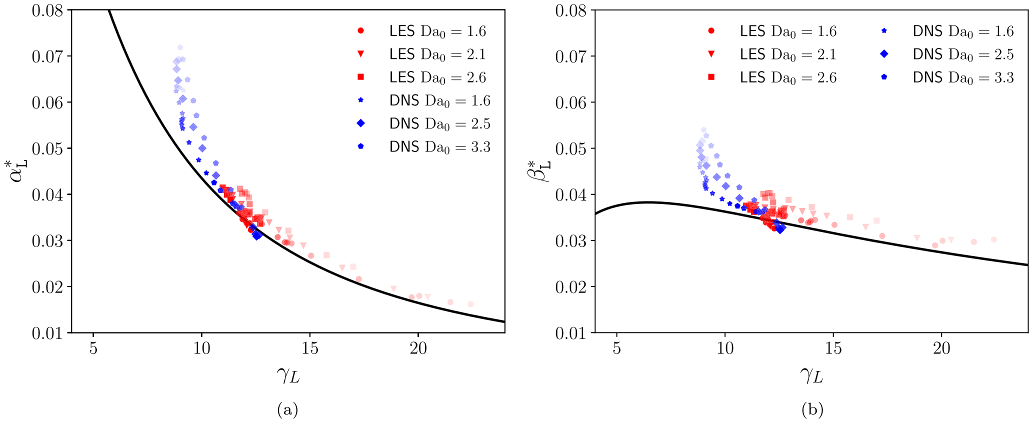

(a)

(b)

FIG. 13. Variations of $\alpha_{\rm L}^\star$ and $\beta_{\rm L}^\star$ defined by Eq. (65) as a function of $\gamma_{\rm L}$. Comparison between simulations results (colored points) and the theoretical prediction (66) with $d_{cc} = 0.55$ (black lines). The simulation points are plotted at different times such that $0.3 < H/L_{\rm dom} < 0.75$ for DNS and $0.2 < H/L_{\rm dom} < 0.75$ for LES. The timeline of the simulation is indicated by the opacity of the symbols: the more opaque, the farther in time. (a) Variations of $\alpha_{\rm L}^\star$ as a function of $\gamma_{\rm L}$. (b) Variations of $\beta_{\rm L}^\star$ as a function of $\gamma_{\rm L}$.

Another point worth mentioning is that, as time increases, the simulation points, whether DNS or LES, converge towards a small region centered around

$$\gamma_\infty \approx 12, \quad \alpha_\infty \approx 0.037, \quad \beta_\infty \approx 0.037. \tag{67}$$

These values are coherent with the fitted parameters (60).

The reason why a convergence occurs towards these values cannot be answered by the analysis presented in this work. Nor can it be said whether this convergence is universal or not. Concerning this last point, we recall that the asymptotic value of $\alpha_{\rm nr}$ obtained in nonreactive Rayleigh-Taylor turbulence is predicted to be independent from large-scale initial conditions [17] : the latter are superseded by nonlinear back-scattering processes and are eventually forgotten. To determine whether a similar conclusion applies for the reactive case, an analysis of the large-scale part of the turbulent spectra of concentration and velocity would be required.

V. CONCLUSIONS

In this work, we studied the relation between the mixing level and the growth of a reactive Rayleigh-Taylor mixing zone. We showed that with less mixing, the width of the mixing zone grows faster. This conclusion is qualitatively the same as the one obtained in the nonreactive case. We also showed that an optimal value of the mixing level exists that maximizes the displacement of the mixing zone center, also congruent with the consumption rate of the reactants. As a result, the flame speed cannot exceed a maximal value determined by the directional anisotropy of turbulent structures.

Quantitative formulas relating the growth and displacement rates, α and β, to the mixing level prefactor γ were derived. In doing so, we also obtained a prediction for the shape of the mean concentration profile. The latter is far from trivial: it is asymmetric and displays two distinct zones, a fast varying one close to reactants and a slow varying trailing edge. All of these predictions were assessed using DNS and LES with a resolution high enough to reach states close to the self-similar regime but still unconfined.

As a perspective, we note that, despite their intrinsic interest, the formulas relating α, β, and γ do not allow us to determine a particular value of these coefficients. Some additional information is required. It could possibly be obtained by studying the very large scales of the flow, as was done in the nonreactive case [17]. This will be the object of future work. As another perspective, we would like to stress that the dominant mode assumption used in this work impacts not only the concentration field but also the velocity field. Thus, additional relation can in principle be obtained to link some properties of the velocity field to the level of mixing. Some of these aspects are discussed in Appendix B. In particular, the value of the constant appearing in turbulent flame speed models is shown to depend on the mixing parameter prefactor γ.

APPENDIX A: ABOUT THE DEFINITIONS OF α AND L

From the start of this study, we focused on the particular definition of L given by Eq. (4): $L = 6\int \overline{c}(1-\overline{c})\,\mathrm{d}x_3$. This definition involves a numerical parameter, 6, and one may wonder why this specific value is important. This question is all the more pressing because α is directly proportional to this prefactor and establishing a relation between α and γ would be pointless if α was defined up to an arbitrary multiplicative constant.

What constrains α in our derivation is the eigenmode analysis detailed in this very section. For the definition of the eigenmodes a_+, a_-, and a_0 to be valid and for relations (44) and (45) to hold, the buoyancy production terms must emulate those of a homogeneous flow. In particular, we must have

$$\langle \overline{u_3'c'}\partial_3\overline{c}\rangle = -\frac{1}{L}\langle\overline{u_3'c'}\rangle, \tag{A1}$$

with a similar relationship for $\overline{c'^2}$. So let us assume temporarily that $L = \delta\int\overline{c}(1-\overline{c})\,\mathrm{d}x_3$ with δ an unknown constant. Then, using the truncated Legendre expansion (25) of $\overline{u_3'c'}$ and knowing that $\partial_3\overline{c} < 0$, we find that

$$\langle \overline{u_3'c'}\partial_3\overline{c}\rangle = \frac{F_0V_L}{L}\int \overline{c}(1-\overline{c})\partial_3\overline{c}\,\mathrm{d}x_3 = -\frac{F_0V_L}{L}\int_0^1 \overline{c}(1-\overline{c})\,d\overline{c} = -\frac{F_0V_L}{6L} \tag{A2a}$$

$$\text{and}\quad \frac{1}{L}\langle\overline{u_3'c'}\rangle = \frac{F_0V_L}{L}\frac{\int\overline{c}(1-\overline{c})\,\mathrm{d}x_3}{L} = \frac{F_0V_L}{\delta L}. \tag{A2b}$$

Thus, to satisfy Eq. (A1), we must have $\delta = 6$. This removes any ambiguity in the definitions of α and L used in this work: they are necessarily associated with the numerical prefactor 6 appearing in the definition (4) of L.

APPENDIX B: ENERGY BUDGET AND FLAME SPEED

In the main text, our analysis has focused almost entirely on the properties of the concentration field and of its mean value $\overline{c}$. This restricted scope was indeed sufficient to achieve our main objective, i.e., deriving Eqs. (49)–(50) and (52)–(54), which link α and β to γ. Still, further interesting information can be gathered by looking at other quantities and in particular at the velocity field and at the turbulent kinetic energy.

Expanding on the results of Ref. [12], the turbulent kinetic energy can be related to the growing mode and by extension to the mixing level γ, just as the concentration flux was in Sec. III C 1. This operation leads to two main outcomes. First, it allows us to examine the energy budget and the dependency of its constitutive terms on γ. Several particular values of γ can thus be identified. Second, it allows us to express the velocity of the flame center as a function of the turbulent velocity: a turbulent flame speed model can thus be formulated.

1. Kinetic energy, potential energy, and dissipation

From Eq. (1b), we derive the following evolution equation for the kinetic energy $\overline{k} = \frac{1}{2}\overline{u_iu_i}$:

$$\partial_t\overline{k} + \partial_3\left(\tfrac{1}{2}\overline{u_3u_iu_i} + \overline{u_3p} - \nu\partial_3\overline{k}\right) = 2\mathtt{A}_t g\overline{u_3c} - \overline{\varepsilon}, \tag{B1}$$

with $\overline{\varepsilon} = \nu\overline{\partial_j u_i \partial_j u_i}$ the dissipation rate of the kinetic energy. Integrating this equation over x_3, the flux term vanishes, and we are left with the following global energy budget:

$$E_K + D_K = E_P, \tag{B2}$$

where E_K is the total kinetic energy, E_P is the potential energy released into the flow, and D_K is the energy dissipated into heat. These energies are hereafter defined per unit volume of the mixing zone:

$$\begin{aligned} E_K(t) &= \frac{1}{H(t)} \int \overline{k}(t, x_3)\, \mathrm{d}x_3, \quad D_K(t) = \frac{1}{H(t)} \int_0^t \int \overline{\varepsilon}(t', x_3)\, \mathrm{d}x_3\, \mathrm{d}t', \\ \text{and} \quad E_P(t) &= \frac{2\mathtt{A}_t g}{H(t)} \int_0^t \int \overline{u_3 c}(t', x_3)\, \mathrm{d}x_3\, \mathrm{d}t', \end{aligned} \tag{B3}$$

where we recall that $H = L/\mathcal{G} > L$ measures the full extent of the turbulent mixing zone, which is larger than the front of size L where the mean concentration varies rapidly. The value of E_P can be deduced from the previous results by substituting $\overline{u_3 c}$ with its assumed expression $F_0(\dot{L})\overline{c}(1-\overline{c})$. In the self-similar regime, we find that

$$E_P = (2\mathtt{A}_t gt)^2 \times \frac{1}{24} \frac{[d_{cc}\mathcal{G}(\gamma)]^2}{1 + d_{cc}\mathcal{G}(\gamma)}. \tag{B4}$$

As for the kinetic energy E_K, it can be expressed by exploiting further the assumption already introduced in Sec. III C and according to which the unstable eigenmode of the Rayleigh-Taylor instability is much larger than the other ones. As shown in [12], this assumption allows us to relate not only α but also the kinetic energy to the mixing level. Extending the results of [12] to the reactive context of this study, we find that, in the self-similar regime, E_K is equal to

$$E_K = (2\mathtt{A}_t gt)^2 \times \frac{1}{12 d_{jj}} \frac{[d_{cc}\mathcal{G}(\gamma)]^3}{[1 + d_{cc}\mathcal{G}(\gamma)]^2}, \tag{B5}$$

where $d_{jj} \in [0, 1]$ is a parameter measuring the anisotropy of the turbulent structures, just as d_{cc} does. As for the total dissipation D_K, its expression can be deduced from the energy budget (B2):

$$D_K = (2\mathtt{A}_t gt)^2 \times \frac{1}{24} \frac{[d_{cc}\mathcal{G}(\gamma)]^2}{1 + d_{cc}\mathcal{G}(\gamma)} \left[1 - \frac{2}{d_{jj}} \frac{d_{cc}\mathcal{G}(\gamma)}{1 + d_{cc}\mathcal{G}(\gamma)}\right]. \tag{B6}$$

2. Maximum dissipation, equipartition of energy, and realizability interval

By linking α and β to γ, Eqs. (49)–(50) and (52)–(54) show that the knowledge of only one of these three parameters is sufficient to define the asymptotic self-similar state of a reactive Rayleigh-Taylor flow. Still, they do not provide any information on the value of this independent parameter. To this end, a study of the large scales of reactive Rayleigh-Taylor turbulence, similar to the one performed in [17], would most probably be required. A particular value of γ was nonetheless identified in the previous analysis: $\gamma_{\max} \approx 6$ is the value of γ for which β reaches its maximum. This value is of course not constraining. However, it still offers a point of reference with which one may assess simulation results. In this regard, the energy budget (B2) allows us to identify additional particular values of γ and to further map out the otherwise indiscriminate interval of γ which extends from 0 to ∞.

Both E_P and E_K are decreasing functions of γ: for higher levels of mixing, less potential energy can be released into the flow and less kinetic energy can be generated. As for the dissipation D_K, it is not necessarily monotonic. Whenever $d_{jj} < 2 - \frac{4}{2+3d_{cc}+d_{cc}^2}$, a mild condition that is always satisfied when $d_{cc} > \sqrt{17}/2 - 3/2 \approx 0.56$, D_K reaches a maximum for $\gamma = \gamma_D$ with

$$\gamma_D = \mathcal{G}^{-1}\left[\frac{1}{2d_{cc}}\left(\sqrt{1+\frac{16}{2-d_{jj}}} - 3\right)\right]. \tag{B7}$$

For the values of d_{cc} and d_{jj} observed in the simulations detailed in Sec. IV, i.e., $d_{cc} \approx d_{jj} \approx 0.55$, this maximum is located at $\gamma_D = 9.4$.

Another point of interest corresponds to the value of γ where as much potential energy is converted into kinetic energy as it is dissipated into heat. This point is reached for $E_K/E_P = 1/2$, i.e., for

$$\gamma_{\text{equi}} = \mathcal{G}^{-1}\left(\frac{1}{d_{cc}}\frac{d_{jj}}{4-d_{jj}}\right). \tag{B8}$$

For $d_{cc} \approx d_{jj} \approx 0.55$, this yields $\gamma_{\text{equi}} \approx 16$. Below this value, the transfer of potential energy to E_K is predominant, while above it, it is the transfer to heat that is larger.

Let us stress that the system we are considering is not at equilibrium and that there is no reason why it should settle to a maximum dissipative state. There is no reason either why an equipartition of energy transfer should exist. Nonetheless, it is still interesting to point out the existence of these two particular states. Their associated γ values, γ_D and γ_{equi}, can indeed serve as references for analyzing simulations. In this regard, it is worth mentioning that, in the nonreactive case, the total dissipation as a function of Θ_∞ reaches a maximum for $\Theta_\infty \approx 0.7$ and that the equality between E_K and D_K is reached for $\Theta_\infty = 0.8$ (see Ref. [12]). In most simulations, the observed self-similar value of Θ is found to lie between those two values. Given the proximity between the reactive and nonreactive cases which we have identified so far, one may wonder whether this observation also holds in the reactive case, i.e., whether the asymptotic value of γ lies in between γ_D and γ_{equi}. The DNS and LES performed in Sec. IV suggest that this is indeed the case: in Fig. 13, γ appears to converge to a value close to 12.

A last point we would like to mention is that not all values of γ are allowed. Indeed, the kinetic energy E_K cannot exceed the potential energy E_P released into the flow. Or equivalently, the dissipation D_K must always be positive. This condition may be verified for all γ provided $d_{cc} < d_{jj}/(2 - d_{jj}) < d_{jj}$. However, the expressions of d_{cc} and d_{jj} obtained in [12] [Eq. (9) in this reference] suggest that we should rather have $d_{jj} \leqslant d_{cc}$. In that case, a constraint applies on the value of γ. The latter must verify

$$\gamma > \gamma_{\text{lim}} \quad \text{with} \quad \gamma_{\text{lim}} = \mathcal{G}^{-1}\left(\frac{d_{jj}}{d_{cc}}\frac{1}{2-d_{jj}}\right). \tag{B9}$$

For $d_{cc} \approx d_{jj} \approx 0.55$, we find that $\gamma_{\text{lim}} = 3.8$. Below this value, no asymptotic state based on the assumptions developed in this work is possible.

3. Dynamical estimate of kinetic energy, potential energy, and dissipation

The results presented so far in this appendix apply at very large times when the mixing rate Θ is asymptotically small. At intermediate times, when Θ is small but not negligible, a prediction of the kinetic energy, of the potential energy, and of the dissipation rate can also be established by considering the dynamical estimates α_{L}, γ_{L} and by assuming the predominance of the Rayleigh-Taylor unstable eigenmode, as discussed in Sec. III C. In addition to this central assumption, the anisotropy constants d_{cc} and d_{jj} and the dynamic estimate γ_{L} are also assumed to reach a constant value at large times. Using the definition $\alpha_{\text{L}} = (\dot{L})^2/(8\mathtt{A}_t gL)$ along with Eqs. (36), (45), and (50) and the relation that links the turbulent kinetic energy and concentration variance exposed in [12], one arrives at

$$E_K = \frac{1}{48 d_{jj} d_{cc} \mathcal{G}(\gamma_{\rm L})} \frac{\dot{L}^2}{1-\Theta}, \tag{B10}$$

$$E_P = \frac{1 + (1-\Theta) d_{cc} \mathcal{G}(\gamma_{\rm L})}{96 d_{cc}^2 \mathcal{G}(\gamma_{\rm L})^2} \frac{\dot{L}^2}{(1-\Theta)^2}. \tag{B11}$$

As for the dissipation, it is deduced from Eqs. (B10) and (B11) due to the global energy budget [Eq. (B2)]:

$$D_K = \frac{d_{jj} + (1-\Theta) d_{cc} \mathcal{G}(\gamma_{\rm L})(d_{jj} - 2)}{96 d_{jj} d_{cc}^2 \mathcal{G}(\gamma_{\rm L})^2} \frac{\dot{L}^2}{(1-\Theta)^2}. \tag{B12}$$

Overall Eqs. (B10), (B11), and (B12) involve Θ and $\gamma_{\rm L}$, two quantities measuring the mixing level. Since our attention is focused on the dependency of E_K, E_P, and D_K on $\gamma_{\rm L}$, we account for the persistent influence of Θ by introducing the following dimensionless version of E_K, E_P, and D_K:

$$E_K^\star = (1-\Theta) \frac{E_K}{\dot{L}^2}, \tag{B13}$$

$$E_P^\star = (1-\Theta)^2 \frac{E_P}{\dot{L}^2}, \tag{B14}$$

$$D_K^\star = (1-\Theta)^2 \frac{D_K}{\dot{L}^2}. \tag{B15}$$

Note that there remains an influence of Θ through higher order terms in $E_P^\star$, $D_K^\star$. Even so, the main advantage of introducing $E_K^\star$, $E_P^\star$, and $D_K^\star$ is that to the main order, they are given by

$$E_K^\star = \frac{1}{48 d_{jj} d_{cc} \mathcal{G}(\gamma_{\rm L})}, \tag{B16}$$

$$E_P^\star \approx \frac{1 + d_{cc} \mathcal{G}(\gamma_{\rm L})}{96 d_{cc}^2 \mathcal{G}(\gamma_{\rm L})^2}, \tag{B17}$$

$$D_K^\star \approx \frac{d_{jj} + d_{cc} \mathcal{G}(\gamma_{\rm L})(d_{jj} - 2)}{96 d_{jj} d_{cc}^2 \mathcal{G}(\gamma_{\rm L})^2}. \tag{B18}$$

As can be seen, the prediction of $E_K^\star$, $E_P^\star$, and $D_K^\star$ involves only $\gamma_{\rm L}$. This makes it easier to check the consistency of Eqs. (B10), Eqs. (B11), and Eqs. (B12) with simulations. Figure 14 illustrates the evolution of $E_K^\star$, $E_P^\star$, and $D_K^\star$ with $\gamma_{\rm L}$ during the "self-similar" interval of time mentioned in Sec. IV D 2. The black curves in Figs. 14(a), 14(b), and 14(c) correspond, respectively, to the theoretical predictions Eqs. (B16), (B17), and (B18). The curves are drawn for $d_{cc} = 0.55$ and $d_{jj} = 0.52$, which are the values found in simulations. Figure 14 shows that, for LES, the trajectories followed by the simulation points are aligned with the theoretical curves. Note also that the simulation points end up concentrating in a small area centered on the values

$$E_K^\star \approx 0.2, \quad E_P^\star \approx 0.3, \quad D_K^\star \approx 0.1. \tag{B19}$$

with $\gamma_{\rm L} \approx 12$ as previously noted. Concerning the DNS, the agreement between simulation points and predictions can also be observed for the potential energy and total dissipation. Final values are roughly the same. However, a discrepancy between the evolution of kinetic energy and prediction can be noted for the cases D3 and D4. A statistical effect might be at the origin of this discrepancy, but further investigation would be required to confirm this possible explanation. Note that, unlike the cases D3 and D4, the case D2, shows a good agreement between the value of $E_K^\star$ computed by Eqs. (B13) and its prediction (B16). Overall, a reasonable agreement is observed between Eqs. (B16), (B17), and (B18) and the kinetic energy, potential energy and total dissipation observed in simulations.

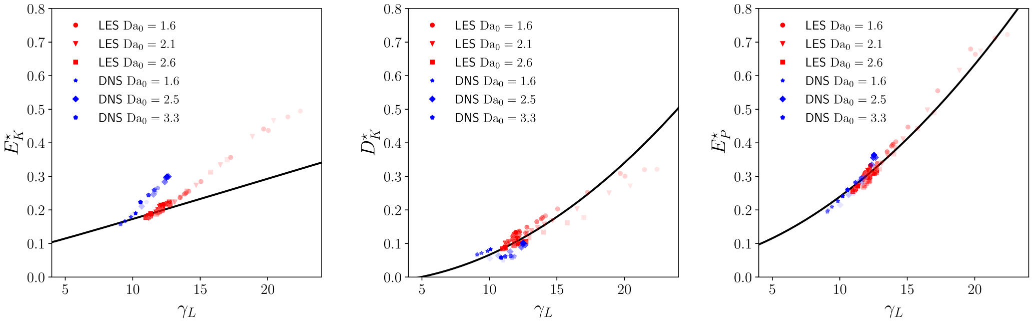

(a) Kinetic energy (b) Dissipation (c) Potential energy

FIG. 14. Variations of $E_K^\star$, $D_K^\star$, and $E_P^\star$, respectively defined by Eqs. (B13), (B15), and (B14), as a function of γ_{L}. Comparison between simulation results (colored points) and the theoretical predictions (B16), (B18), and (B17) with $d_{cc} = 0.55$ and $d_{jj} = 0.52$ (black lines). The simulation points are plotted at different times such that $0.3 < H/L_{\mathrm{dom}} < 0.75$ for DNS and $0.2 < H/L_{\mathrm{dom}} < 0.75$ for LES. The timeline of the simulation is indicated by the opacity of the symbols: the more opaque, the farther in time.

4. Flame speed

The flame speed associated with the displacement of the mixing zone center is defined by

$$s_c = \dot{X}_c. \tag{B20}$$

A turbulent velocity representative of the maximum value of the kinetic energy profile is

$$\upsilon' = \sqrt{\langle \bar{k} \rangle} = \sqrt{\frac{H}{L} E_K}. \tag{B21}$$

Using Eqs. (5), (52), and (B5), we then deduce that, at asymptotic times when Θ can be neglected, we have

$$s_c = C_f \upsilon' \quad \text{with} \quad C_f = \sqrt{\frac{d_{jj} d_{cc}}{3} \gamma \mathcal{G}(\gamma)}. \tag{B22}$$

Thus, the burning velocity s_c scales linearly with the turbulent velocity υ' in the self-similar regime. This is consistent with Damköhler's theory [40].

As can be seen, in Fig. 15, the prefactor C_f of this proportionality law increases with γ. Note also that the prefactor C_f is bounded by

$$C_f < \sqrt{12 d_{jj} d_{cc}}. \tag{B23}$$

With $d_{cc} \approx d_{jj} \approx 0.55$, this corresponds to a maximum value of approximately 2.

At intermediate times, when Θ is not yet negligible, Eq. (B22) still holds but C_f is modified. The dominant mode assumption [Eq. (40)] along with Eqs. (13)–(50) leads to

$$C_f(t) = \sqrt{\frac{(1 - \Theta) d_{jj} d_{cc}}{3} \gamma_{\mathrm{L}} \mathcal{G}(\gamma_{\mathrm{L}})}. \tag{B24}$$

The dependency of this expression on Θ can be set apart by introducing a reduced version of the turbulent flame speed:

$$s_c^\star = \frac{s_c}{\sqrt{1 - \Theta}}. \tag{B25}$$

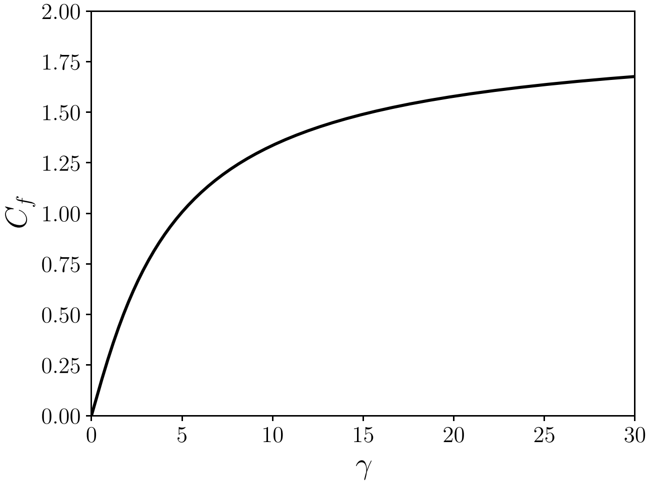

FIG. 15. Evolution of C_f with γ for $d_{cc} = 0.55$ and $d_{jj} = 0.52$.

This reduced flame speed s_c^* is predicted to be proportional to υ', with a constant $C_f^\star$ that depends on γ_L but not on Θ:

$$s_c^\star = C_f^\star \upsilon' \quad \text{with} \quad C_f^\star = \sqrt{\frac{d_{jj} d_{cc}}{3}} \gamma_\mathrm{L} \mathcal{G}(\gamma_\mathrm{L}). \tag{B26}$$

Figure 16 shows the evolution of $C_f^\star$ extracted from simulations using Eq. (B25) with respect to γ_L computed with Eq. (6). The black curve corresponds to the prediction Eq (B26). The latter is plotted for $d_{cc} = 0.55$ and $d_{jj} = 0.52$. The comparison between simulations and prediction is done for DNS, D2, D3, D4 and LES L2,L3, L4. As can be seen, the simulation points of D2, L2, L3,

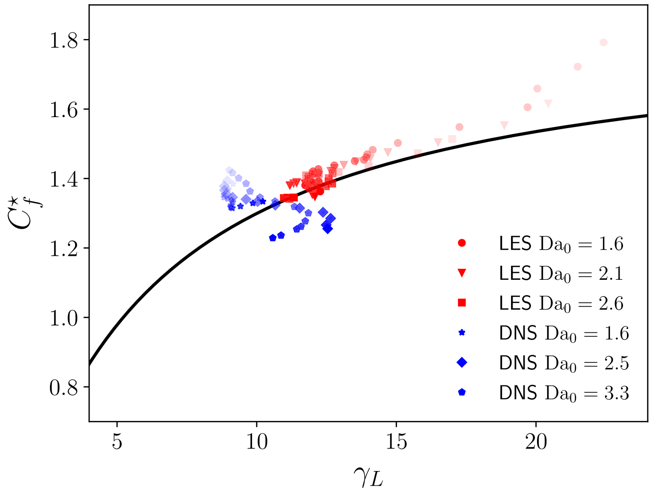

FIG. 16. Variations of $C_f^\star = s_c^\star/\upsilon'$, defined by Eq. (B25), as a function of γ_L. Comparison between simulation results (colored points) and the theoretical prediction (B26) with $d_{cc} = 0.55$ and $d_{jj} = 0.52$ (black lines). The simulation points are plotted at different times such that $0.3 < H/L_\mathrm{dom} < 0.75$ for DNS and $0.2 < H/L_\mathrm{dom} < 0.75$ for LES. The timeline of the simulation is indicated by the opacity of the symbols: the more opaque, the farther in time.

L4 all tend to the black curve. On the contrary, there remains a small deviation for simulations D3 and D4. This deviation is less than 15% of the value that would be obtained with Eq. (B26). To explain this deviation, there might be a statistical effect at play which is already manifest for the kinetic energy (see Sec. B 3). Even so, Fig. 16 seems to indicate that the result of Eq. (B26) agrees well with simulations. An another important remark that can be made is that the simulation points accumulate on a small region where the prefactor $C_f^\star$ takes the value

$$C_f^\star = 1.35. \tag{B27}$$

To conclude the discussion on this topic, we would like to point out that the turbulent flame speed model determined for the self-similar regime Eq. (B22) can be recast in the form

$$s_c = \frac{d_{cc}\gamma\mathcal{G}(\gamma)}{6\sqrt{1+d_{cc}\mathcal{G}(\gamma)}}\sqrt{2\mathtt{A}_t gL} \approx \sqrt{0.138\times 2\mathtt{A}_t gL}, \tag{B28}$$

where the last approximation is obtained by replacing γ and d_{cc} with their asymptotic values observed in simulations. This alternative formulation of Eq. (B22) is almost similar to the one proposed in Refs. [27,32]. However, it should be noted that, in these references, the size L_{dom} of the domain is used instead of the size L of the mixing zone. This is possible because the configuration studied in these references is confined, as opposed to the one studied here.

APPENDIX C: SOURCE TERM MODIFICATION

In this appendix, we assume that the $c(1-c)$ dependency of the F-KPP reactive source term is replaced by a general function $R(c)$ verifying

$$\text{for} \quad c\in]0,1[, \quad R(c)>0, \quad \text{and} \quad R(0)=R(1)=0. \tag{C1}$$

In system (1), the evolution (1a) of the concentration field would then be replaced by

$$\partial_t c + u_k\partial_k c = \nu_c\partial_{kk}^2 c + \frac{1}{\tau}R(c). \tag{C2}$$

The core assumption of this appendix is that this substitution does not modify the main characteristics of the flow in the self-similar regime. In particular, we assume that L and X_c still grow as the square of time and that a thickened-wrinkled flame regime is reached, such that the flow becomes more and more segregated.

To extend the results of this work to this situation, the idea is to introduce another measure of the mixing level. Instead of Θ, we define

$$\Theta^\diamond(t) = \frac{\int \overline{R}(x_3,t)\,\mathrm{d}x_3}{\int \overline{c}(1-\overline{c})(x_3,t)\,\mathrm{d}x_3} > 0. \tag{C3}$$

This quantity is positive but has an upper bound which is not necessarily equal to 1, as opposed to Θ. Nonetheless, like Θ, $\Theta^\diamond$ tends to 0 when the mixture tends to a fully segregated state. In particular, it should verify the same self-similar asymptotic scaling as Θ, but with a different constant:

$$\text{self-similar regime: } \Theta^\diamond(t) = \gamma^\diamond\frac{\tau}{t}. \tag{C4}$$

The interest of introducing $\Theta^\diamond$ is that all the steps of the derivation detailed in the main text can be repeated by simply replacing Θ with $\Theta^\diamond$ and γ with $\gamma^\diamond$. Thus, the main predictions of this work, Eqs. (49) and (52), would become

$$\alpha = \frac{[d_{cc}\mathcal{G}(\gamma^\diamond)]^2}{1+d_{cc}\mathcal{G}(\gamma^\diamond)} \quad \text{and} \quad \beta = \frac{\gamma^\diamond}{12}\frac{[d_{cc}\mathcal{G}(\gamma^\diamond)]^2}{1+d_{cc}\mathcal{G}(\gamma^\diamond)}. \tag{C5}$$

Their dynamic versions, Eqs. (50) and (54), would be transformed alike:

$$\alpha_{\mathrm{L}} = \frac{[d_{cc}(1-\Theta^\diamond)\mathcal{G}(\gamma_{\mathrm{L}}^\diamond)]^2}{1+d_{cc}(1-\Theta^\diamond)\mathcal{G}(\gamma_{\mathrm{L}}^\diamond)} \quad \text{and} \quad \beta_{\mathrm{L}} = \frac{\gamma_{\mathrm{L}}^\diamond}{12}\frac{[d_{cc}(1-\Theta^\diamond)\mathcal{G}(\gamma_{\mathrm{L}}^\diamond)]^2}{1+d_{cc}(1-\Theta^\diamond)\mathcal{G}(\gamma_{\mathrm{L}}^\diamond)}, \tag{C6}$$

with $\gamma_{\mathrm{L}}^\diamond(t) = 2\Theta^\diamond(t)\frac{\tau_L(t)}{\tau}$.

The comparison with the main text results can be pushed further by introducing an additional hypothesis. The probability density function (PDF) of a scalar bounded between 0 and 1 is usually well described by a β-PDF. We assume that this is the case for reactive RayleighTaylor turbulence, that is to say, we assume that the PDF of c is

$$f_\beta(c) = \frac{c^{a-1}(1-c)^{b-1}}{B(a,b)} \quad \text{with} \quad a = \overline{c}\frac{\overline{c(1-c)}}{\overline{c'^2}}, \quad b = (1-\overline{c})\frac{\overline{c(1-c)}}{\overline{c'^2}},$$

$$B(a,b) = \int_0^1 c^{a-1}(1-c)^{b-1}\,\mathrm{d}c. \tag{C7}$$

The function $B(a,b)$ is the β-function and is equal to $\Gamma(a)\Gamma(b)/\Gamma(a+b)$, with Γ the extension of the factorial to positive reals. In the limit $\Theta \ll 1$ and with the assumption that $\overline{c(1-c)}$ varies like $\overline{c}(1-\overline{c})$, the two parameters a and b tend to

$$\text{for} \quad \Theta \ll 1, \quad a \approx \overline{c}\Theta, \quad \text{and} \quad b \approx (1-\overline{c})\Theta. \tag{C8}$$

As a result, the average of R can be expressed as

$$\text{for} \quad \Theta \ll 1, \quad \overline{R} = \int_0^1 R(c)f_\beta(c)\,\mathrm{d}c \approx \frac{\mathcal{R}(\overline{c},\Theta)}{B(\overline{c}\Theta,(1-\overline{c})\Theta)} \quad \text{with}$$

$$\mathcal{R}(\overline{c},\Theta) = \int_0^1 R(c)c^{a-1}(1-c)^{b-1}\,\mathrm{d}c. \tag{C9}$$

For small values of Θ, the β-function $B(a,b)$ diverges as

$$\text{for} \quad \Theta \ll 1, \quad B(a,b) \approx [\overline{c}(1-\overline{c})\Theta]^{-1}. \tag{C10}$$

By contrast, with $R(0) = R(1) = 0$, the integral $\mathcal{R}(\overline{c},\Theta)$ tends to a finite value:

$$\text{for} \quad \Theta \ll 1, \quad \mathcal{R}(\overline{c},\Theta) \approx \mathcal{R}(\overline{c},0). \tag{C11}$$

Therefore, injecting the above expression into the definition of $\Theta^\diamond$, one deduces that

$$\text{for} \quad \Theta \ll 1, \quad \overline{R} \approx \Theta\overline{c}(1-\overline{c})\mathcal{R}(\overline{c},0), \tag{C12}$$

and that

$$\text{for} \quad \Theta \ll 1, \quad \Theta^\diamond \approx \eta^\diamond\Theta \quad \text{with} \quad \eta^\diamond = \frac{\int \overline{c}(1-\overline{c})\mathcal{R}(\overline{c},0)\,\mathrm{d}x_3}{\int \overline{c}(1-\overline{c})\,\mathrm{d}x_3}. \tag{C13}$$

Thus, Θ and $\Theta^\diamond$ are proportional to one another, with a prefactor that depends on the shape $R(c)$ of the source term and that can be determined analytically or numerically depending on the complexity of $R(c)$. This proportionality relationship can be used to replace $\Theta^\diamond$ and $\gamma^\diamond$ in Eqs. (C5) and (C6). One finds that

$$\alpha = \frac{[d_{cc}\mathcal{G}(\eta^\diamond\gamma)]^2}{1+d_{cc}\mathcal{G}(\eta^\diamond\gamma)} \quad \text{and} \quad \beta = \frac{\eta^\diamond\gamma}{12}\frac{[d_{cc}\mathcal{G}(\eta^\diamond\gamma)]^2}{1+d_{cc}\mathcal{G}(\eta^\diamond\gamma)}, \tag{C14a}$$

$$\alpha_{\mathrm{L}} = \frac{[d_{cc}(1-\eta^\diamond\Theta)\mathcal{G}(\eta^\diamond\gamma_{\mathrm{L}})]^2}{1+d_{cc}(1-\eta^\diamond\Theta)\mathcal{G}(\eta^\diamond\gamma_{\mathrm{L}})} \quad \text{and} \quad \beta_{\mathrm{L}} = \frac{\eta^\diamond\gamma_{\mathrm{L}}}{12}\frac{[d_{cc}(1-\eta^\diamond\Theta)\mathcal{G}(\eta^\diamond\gamma_{\mathrm{L}})]^2}{1+d_{cc}(1-\eta^\diamond\Theta)\mathcal{G}(\eta^\diamond\gamma_{\mathrm{L}})}. \tag{C14b}$$

To illustrate how $\eta^\diamond$ depends on the shape of R, we may look at the particular case where R varies like

$$R(c) = c^m(1-c)^n. \tag{C15}$$

Then, in the limit $\Theta \ll 1$, we have $\overline{R} = \overline{c}(1-\overline{c})\Theta B(m,n)$ so that $\eta^\diamond$ is equal to

$$\eta^\diamond = B(m,n). \tag{C16}$$

With m and n decreasing below 1, the profile of $R(c)$ becomes flatter than in the F-KPP case ($m = n = 1$) (ultimately, it tends to a steplike profile when m and n tend to 0). In that case, Eq. (C16) shows that $\eta^\diamond$ becomes larger than 1 and increases as m and n decrease. For a given level of mixing measured by γ, α is then smaller than in the F-KPP case. By contrast, with m and n increasing above 1, the profile of $R(c)$ becomes more peaked and $\eta^\diamond$ decreases. For a given level of mixing measured by γ, α is then higher than in the F-KPP case.

[1] D. H. Sharp, An overview of Rayleigh-Taylor instability, Physica D **12**, 3 (1984).

[2] H.-J. Kull, Theory of the Rayleigh-Taylor instability, Phys. Rep. **206**, 197 (1991).

[3] G. Boffetta and A. Mazzino, Incompressible Rayleigh-Taylor turbulence, Ann. Rev. Fluid Mech. **49**, 119 (2017).

[4] Y. Zhou, Rayleigh–Taylor and Richtmyer–Meshkov instability induced flow, turbulence, and mixing. I, Phys. Rep. **720–722**, 1 (2017).

[5] Y. Zhou, Rayleigh–Taylor and Richtmyer–Meshkov instability induced flow, turbulence, and mixing. II, Phys. Rep. **723–725**, 1 (2017).

[6] D. L. Youngs, Numerical simulation of turbulent mixing by Rayleigh-Taylor instability, Physica D **12**, 32 (1984).

[7] G. Dimonte, D. L. Youngs, A. Dimits, S. Weber, M. Marinak, S. Wunsch, C. Garasi, A. Robinson, M. J. Andrews, P. Ramaprabhu *et al.*, A comparative study of the turbulent Rayleigh-Taylor instability using high-resolution three-dimensional numerical simulations: The Alpha-Group collaboration, Phys. Fluids **16**, 1668 (2004).

[8] P. Ramaprabhu and M. J. Andrews, Experimental investigation of Rayleigh–Taylor mixing at small Atwood numbers, J. Fluid Mech. **502**, 233 (2004).

[9] G. Dimonte, Dependence of turbulent Rayleigh-Taylor instability on initial perturbations, Phys. Rev. E **69**, 056305 (2004).

[10] P. Ramaprabhu, G. Dimonte, and M. J. Andrews, A numerical study of the influence of initial perturbations on the turbulent Rayleigh-Taylor instability, J. Fluid Mech. **536**, 285 (2005).

[11] B.-J. Gréa, The rapid acceleration model and growth rate of a turbulent mixing zone induced by Rayleigh-Taylor instability, Phys. Fluids **25**, 015118 (2013).

[12] O. Soulard, J. Griffond, and B.-J. Gréa, Influence of the mixing parameter on the second order moments of velocity and concentration in Rayleigh-Taylor turbulence, Phys. Fluids **28**, 065107 (2016).

[13] W. H. Cabot and A. W. Cook, Reynolds number effects on Rayleigh-Taylor instability with possible implications for type Ia supernovae, Nat. Phys. **2**, 562 (2006).

[14] O. Poujade and M. Peybernes, Growth rate of Rayleigh-Taylor turbulent mixing layers with the foliation approach, Phys. Rev. E **81**, 016316 (2010).

[15] D. Livescu, T. Wei, and M. R. Petersen, Direct numerical simulations of Rayleigh–Taylor instability, J. Phys.: Conf. Ser. **318**, 082007 (2011).

[16] D. L. Youngs, The density ratio dependence of self-similar Rayleigh–Taylor mixing, Phil. Trans. R. Soc. A **371**, 20120173 (2013).

[17] O. Soulard, J. Griffond, and B.-J. Gréa, Large-scale analysis of unconfined self-similar Rayleigh-Taylor turbulence, Phys. Fluids **27**, 095103 (2015).

[18] C. Almarcha, P. Trevelyan, P. Grosfils, and A. De Wit, Chemically driven hydrodynamic instabilities, Phys. Rev. Lett. **104**, 044501 (2010).

[19] C. Almarcha, Y. R'Honi, Y. De Decker, P. M. J. Trevelyan, K. Eckert, and A. De Wit, Convective mixing induced by acid-base reactions, J. Phys. Chem. B **115**, 9739 (2011).

[20] A. De Wit, Miscible density fingering of chemical fronts in porous media: Nonlinear simulations, Phys. Fluids **16**, 163 (2004).

[21] M. De Paoli, V. Giurgiu, F. Zonta, and A. Soldati, Universal behavior of scalar dissipation rate in confined porous media, Phys. Rev. Fluids **4**, 101501(R) (2019).

[22] P. Trevelyan, C. Almarcha, and A. De Wit, Buoyancy-driven instabilities around miscible $A + B \to C$ reaction fronts: A general classification, Phys. Rev. E **91**, 023001 (2015).

[23] A. De Wit, Chemo-hydrodynamic patterns and instabilities, Ann. Rev. Fluid Mech. **52**, 531 (2020).

[24] N. Attal and P. Ramaprabhu, The stability of reacting single-mode Rayleigh–Taylor flames, Physica D **404**, 132353 (2020).

[25] B. E. Morgan, B. J. Olson, W. J. Black, and J. A. McFarland, Large-eddy simulation and Reynolds-averaged Navier-Stokes modeling of a reacting Rayleigh-Taylor mixing layer in a spherical geometry, Phys. Rev. E **98**, 033111 (2018).

[26] B. E. Morgan, Simulation and Reynolds-averaged Navier-Stokes modeling of a three-component Rayleigh-Taylor mixing problem with thermonuclear burn, Phys. Rev. E **105**, 045104 (2022).

[27] A. M. Khokhlov, Propagation of turbulent flames in supernovae, Astrophys. J. **449**, 695 (1995).

[28] M. Zingale, S. E. Woosley, C. A. Rendleman, M. S. Day, and J. B. Bell, Three-dimensional numerical simulations of Rayleigh-Taylor unstable flames in type Ia supernovae, Astrophys. J. **632**, 1021 (2005).

[29] N. Vladimirova, Model flames in the Boussinesq limit: rising bubbles, Combust. Theory Model. **11**, 377 (2006).

[30] M. Chertkov, V. Lebedev, and N. Vladimirova, Reactive Rayleigh-Taylor turbulence, J. Fluid Mech. **633**, 1 (2009).

[31] E. P. Hicks and R. Rosner, Gravitationally unstable flames: Rayleigh–Taylor stretching versus turbulent wrinkling, Astrophys. J. **771**, 135 (2013).

[32] E. P. Hicks, Rayleigh–Taylor unstable flames—Fast or faster?, Astrophys. J. **803**, 72 (2015).

[33] E. P. Hicks, Rayleigh-Taylor unstable flames at higher Reynolds number, Mon. Not. R. Astron. Soc **489**, 36 (2019).

[34] M. Liu and E. P. Hicks, Rayleigh–Taylor unstable flames: The coupled effect of multiple perturbations, arXiv:2309.15046.

[35] D. T. Casey, V. A. Smalyuk, R. E. Tipton, J. E. Pino, G. P. Grim, B. A. Remington, D. P. Rowley, S. V. Weber, M. Barrios, L. R. Benedetti *et al.*, Development of the CD Symcap platform to study gas-shell mix in implosions at the National Ignition Facility, Phys. Plasmas **21**, 092705 (2014).

[36] R. Borghi and M. Destriau, *La combustion et les flammes* (Éditions Technip, Paris, 1995).

[37] A. Briard, L. Gostiaux, and B.-J. Gréa, The turbulent faraday instability in miscible fluids, J. Fluid Mech. **883**, A57 (2020).

[38] S. Shanmuganathan, D. L. Youngs, J. Griffond, B. Thornber, and R. J. R. Williams, Accuracy of high-order density-based compressible methods in low Mach vortical flows, Int. J. Numer. Meth. Fluids **74**, 335 (2013).

[39] B. Thornber, J. Griffond, O. Poujade, N. Attal, H. Varshochi, P. Bigdelou, P. Ramaprabhu, B. Olson, J. Greenough, Y. Zhou *et al.*, Late-time growth rate, mixing, and anisotropy in the multimode narrowband Richtmyer-Meshkov instability: The θ-group collaboration, Phys. Fluids **29**, 105107 (2017).

[40] G. Damköhler, Der Einfluss der Turbulenz auf die Flammengeschwindigkeit in Gasgemischen, Z. Elektrochem. Angew. Phys. Chem. **46**, 601 (1940).